GEORG-AUGUST-UNIVERSITÄT
GÖTTINGEN

Fakultät für
Physik

Bachelor's Thesis

Abschätzung der systematischen Unsicherheiten einer direkten Top Quark Zerfallsbreitenmessung im $t\bar{t} \rightarrow$ Lepton+Jets-Kanal bei ATLAS

Evaluation of systematic uncertainties for a direct Top Quark decay width measurement in the $t\bar{t} \rightarrow$ lepton+jets-channel at ATLAS

prepared by

Marcel Niemeyer

from Lingen

at the II. Physikalisches Institut

Thesis number:	II.Physik-UniGö-BSc-2016/04
Thesis period:	4th April 2016 until 11th July 2016
First referee:	Prof. Dr. Arnulf Quadt
Second referee:	Prof. Dr. Ariane Frey

Abstract

A precise measurement of the top quark decay width Γ_t is important to study the possibilities of physics beyond the Standard Model, but a direct measurement of this quantity is affected by many sources of uncertainties. Previous measurements at CDF could restrain the value to an interval $1.10\,\text{GeV} < \Gamma_t < 4.05\,\text{GeV}$ [1]. Unlike in the CDF measurement, the modelling of the initial- and final-state radiation contribute the most. The purpose of this thesis is a feasibility study, if the radiation uncertainty can be reduced by applying cuts on observables and kinematic variables. This thesis will validate the used template method as the fit method and prove that cuts can reduce the uncertainty on the fitted decay width. Cuts are studied by comparison of the nominal sample with radiation samples and through systematic scans of the ranges of selected observables and variables.

Zusammenfassung

Eine präzise Messung der Top Quark Zerfallsbreite Γ_t bietet die Möglichkeit zur Entdeckung neuer Physik jenseits des Standard Modells. Jedoch konnte die Zerfallsbreite in einer direkten Messung am CDF Detektor bisher nur auf ein Intervall $1.10\,\text{GeV} < \Gamma_t < 4.05\,\text{GeV}$ eingeschränkt werden [1]. Um eine genauere Messung anbieten zu können, ist es notwendig, in der Messung vorhandene Unsicherheiten zu minimieren. Anders als bei der CDF-Messung, betrifft dies bei dieser Analyse vor allem die Strahlungsunsicherheit, hervorgerufen durch die numerische Modellierung der Strahlung in Ausgangs- und Endzuständen der Reaktion. Diese Arbeit widmet sich der Reduzierung dieser Unsicherheit durch Schnitte auf die Verteilungen der Observablen und kinematischen Variablen. Die Wahl der Schnitte erfolgt über den Vergleich der nominellen Verteilungen mit Verteilungen die ein höheres- oder niedrigeres Maß an Strahlung miteinbeziehen. Eine Optimierung wird mittels eines Scans der Wertebereiche der Observablen bzw. Variablen durchgeführt. Das Ergebnis dieser Arbeit wird sein, dass sich die Unsicherheiten durch gezieltes schneiden reduzieren lassen.

Contents

Nomenclature

Variables

Variable	Meaning	Unit
$\sqrt{s}$	Center of mass energy	eV
$\sqrt{\hat{s}}$	Effective center of mass energy	eV
x	Bjorken x	-
L_ℓ	Lepton number	-
Q	Electric charge	C
Q^2	Momentum transfer	GeV^2
BR	Branching ratio	-
s	Spin	$\hbar$
α_S	Strong coupling constant	-
T	Isospin	-
T_3	Third component of isospin	-
Y	Hypercharge	-
Γ	Decay width	eV
m or M	Mass	eV
τ	Average lifetime	s
$\not{E}_T$	Missing transverse energy	eV
$\mathcal{L}$	Luminosity	$\mathrm{cm}^{-2}\mathrm{s}^{-1}$
η	Pseudorapidity	-
y	Rapidity	-
ε_b	B-tag efficiency	-
p_T	Transverse momentum	GeV
m_T	Transverse mass	GeV
σ	Uncertainty	variable
R_{SC}	(number of signal events)/(number of combined events)	
R_{signal}	(number of signal events with cut)/(number of signal events without cut)	

Constants

Constant	Meaning	Value
c	Speed of light (vacuum)	1
$\hbar$	Planks constant	1
e	Elementary charge	$1.6 \times 10^{-19}\,\mathrm{C}$
G_f	Fermi coupling constant	$1.17 \times 10^{-5}\,\mathrm{GeV}^{-2}$

Particles

Symbol	Particle
ℓ	Charged Lepton
$e^{\mp}$	Electron/Positron
μ^-	Muon
τ^-	Tauon
ν_ℓ	Neutrino
u	Up quark
d	Down quark
c	Charm quark
s	Strange quark
t	Top quark
b	Bottom quark
p	Proton
$W^{\pm}$	W boson
Z	Z boson

Abbreviations

Abbreviation	Meaning
e.g.	exempli gratia, for example
SM	Standard Model
CKM	Cabibbo-Kobayashi-Maskawa
CME	Center of mass energy
MC	Monte Carlo
Θ_W	Weinberg angle

Abbreviation	**Meaning**
JVF	Jet Vertex Fraction
CERN	Conseil Européen pour la Recherche Nucléaire
LHC	Large Hadron Collider
ATLAS	A Toroidal LHC ApparatuS
CMS	Compact Muon Solenoid
ALICE	A Large Ion Collider Experiment
LHCb	LHC Beauty
LAr	Liquid Argon
PDF	Probability distribution function
ID	Identification
SF	Scale Factor
LL	Logarithmic Likelihood
nLL	negative Logarithmic Likelihood
JES	Jet Energy Scale
JER	Jet Energy Resolution
UE	Underlying Events
ISR	Initial State Radiation
FSR	Final State Radiation
CR	Colour Reconnection
KLFitter	Kinematic Likelihood Fitter
P	Probability
Reco.	Reconstructed

Observables

Observables	**Definition**	**Unit**
m_t	m_t^{reco}	eV
D_{32}	$m_t^{\text{reco}} - m_W^{\text{reco}}$	eV
R_{32}	$(m_t^{\text{reco}})/(m_W^{\text{reco}})$	-
R_{diff}	$(m_t^{\text{reco}} - m_W^{\text{reco}})/(\bar{m}_W^{\text{reco}})$	-
$m_{\ell b}$	$m_{\ell b}^{\text{reco}}$	eV

1. Introduction

Particle physics' goal is "to perceive whatever holds, the world together in its inmost folds"[1], something that kept physicists busy for many years. In the last decades, many particles were discovered and a model was developed, the Standard Model of Particle Physics (SM), that describes the microcosm better than any other model so far. The top quark has a special role in the SM. It is by far the heaviest quark, which enables it to decay into particles that other quarks can not decay into. Because of the huge mass, it has the shortest lifetime out of all quarks. This gives a unique possibility to measure quark properties and maybe discover physics beyond the Standard Model, as it will be described in Ch. 2. The chapter gives a brief summary of the physics of the Standard Model and the properties of the top quark, as well as its production in particle colliders and its decay channels. The third chapter will introduce the particle accelerator LHC and its detector ATLAS, which was used to collect the data used in the analysis. After that, the event selection with the PlotFactory package of the Göttingen Top Group will be explained and a short overview over the used ROOT framework will be given. Further, it will be described how the events recorded with ATLAS are reconstructed using the KLFitter framework in Ch. 4. The direct measurement of the top quark decay width will be explained in Ch. 5. It will be stated how the template method that is used in this analysis works and how it is implemented as C++-based code. Additionally, the most important systematic uncertainties affecting the measurement are briefly explained and the observables used in the analysis are introduced and explained. Ch. 6 will state the results of the thesis. Focussing on the radiation uncertainty, it will describe its estimation and the attempts that were made to reduce it.

[1] Johann W. v. Goethe, Faust

2. Theoretical Overview

This chapter is dedicated to the introduction the fundamental aspects of the SM and the production and decay of the top quark as well as its physical properties.

2.1. The Standard Model of Particle Physics

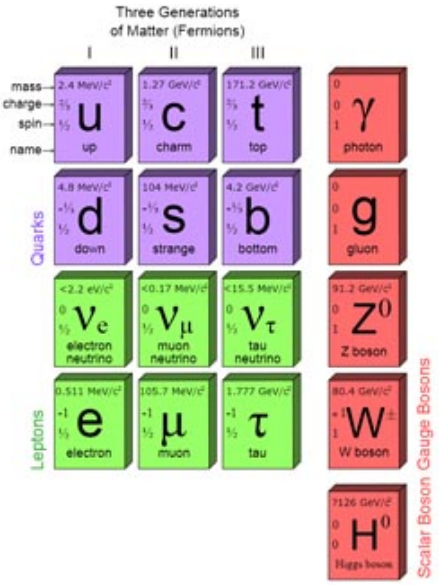

Figure 2.1.: An overview of the particles contained in the SM. Each particle is labelled with its properties like mass and electric charge.

The SM describes the interaction between elementary particles, the fundamental building blocks of matter, in terms of the electromagnetic force, the weak force and the strong force. Gravitation is not included in the SM. There are overall three kinds of elementary particles: quarks, leptons and gauge bosons, mediating the three forces. Quarks and leptons have both spin $s = \frac{1}{2}$, thus are fermions. There is a total of six leptons and quarks, respectively. Leptons are classified by their charge (Q), and lepton specific quantum numbers, called electron number (L_e), muon number (L_μ) and tau number (L_τ).

Analogously, quarks are divided into six flavours, by their charge and six quantum numbers called upness (U), downness (D), strangeness (S), charm (C), bottomness (B) and topness (T). All particles and their quantum numbers are listed in Table 2.1. There is also an antiparticle for each particle, with reversed signs in each quantum number. Using these classifications, quarks and leptons are falling into three generations. Each generation contains two quarks and two leptons arranged in doublets. Quark doublets consist of one up-type quark (u, c, t) with charge $Q = \frac{2}{3}$e and one down-type quark (d, s, b) with charge $Q = -\frac{1}{3}$e. Lepton doublets consist of one neutrino (ν_e, ν_μ, ν_τ) and one charged lepton (e^-, μ^-, τ^-), each with charge $Q = -$e. The properties of each particle and the associated generations are summarised in Fig. 2.1. The SM is described by the gauge

Leptons	L_e	L_μ	L_τ	Q [e]	Quarks	U	D	C	S	T	B	Q [e]
ν_e	1	0	0	0	u	1	0	0	0	0	0	+2/3
e^-	1	0	0	-1	d	0	-1	0	0	0	0	-1/3
ν_μ	0	1	0	0	c	0	0	1	0	0	0	+2/3
μ^-	0	1	0	-1	s	0	0	0	-1	0	0	-1/3
ν_τ	0	0	1	0	t	0	0	0	0	1	0	+2/3
τ^-	0	0	1	-1	b	0	0	0	0	0	-1	-1/3

Table 2.1.: An overview of the charges and particle specific quantum numbers of quarks and leptons. The corresponding antiparticles have the opposite sign.

symmetry

$$SU(3)_C \otimes SU(2)_L \otimes U(1)_Y. \tag{2.1}$$

It is the tensor product of $U(1)$, the gauge symmetry of the electromagnetic force, $SU(2)$, the gauge symmetry of the weak force, and $SU(3)$, the gauge symmetry of the strong force [2].

2.1.1. Strong Interaction

The strong interaction acts between particles with a colour charge. There are three different colour charges, named red (r), blue (b) and green (g) for particles and antired ($\bar{r}$), antiblue ($\bar{b}$) and antigreen ($\bar{g}$) for antiparticles. The gauge symmetry $SU(3)_C$, with the C referring to colour, of the strong force has 8 generators, the so called Gell-Mann-Matrices, and therefore 8 associated gluon fields, as the gluon is the gauge boson of the strong force. Because the $SU(3)_C$ is a non-Abelian group, the gluons carry colour charges

themselves. The potential of the strong force

$$V(\vec{r}) = -\frac{4}{3}\frac{\alpha_S}{r} + \kappa r \tag{2.2}$$

contains a linear term, that gets dominant for large distances. Therefore, the work needed to separate two colour charged particles increases with the distance, until it reaches a point where it is energetically favourable to create a new pair of quarks to reduce the distance. The process of creating quarks is called hadronisation. This causes that every free particle must be colourless, a property called confinement. Colourless particles consist of a combination of all three colours or anticolours, respectively, or the combination of a colour and its anticolour.

2.1.2. Electroweak Interaction

The electromagnetic force is described by the symmetry group $U(1)$, which has only one generator and therefore one gauge boson, the photon. The associated charge is the electric charge, which is not carried by the photon itself.

The weak force is described by $SU(2)$ with three generators and therefore three gauge bosons. Regarding the weak force, all left handed particles are sorted into doublets and all right handed particles into singlets, see Tab. 2.2. The charged $W^{\pm}$ bosons interact with the particles in the doublets, by transforming one into the other. The weak eigenstates d', s' and b' differ from the mass eigenstates d, s and b, and are linked via the Cabibbo-Kobayashi-Maskawa-matrix (CKM-matrix):

$$\begin{pmatrix} d' \\ s' \\ b' \end{pmatrix} = \begin{pmatrix} V_{ud} & V_{us} & V_{ub} \\ V_{cd} & V_{cs} & V_{cb} \\ V_{td} & V_{ts} & V_{tb} \end{pmatrix} \cdot \begin{pmatrix} d \\ s \\ b \end{pmatrix}. \tag{2.3}$$

The CKM-matrix has four free parameters, including one complex phase factor [3]. The complex phase factor is the reason for CP violation in the SM.

To combine the electromagnetic force and the weak force to the electroweak force, a weak hypercharge $Y = 2(Q - T_3)$ is introduced. The weak hypercharge generates the same group $U(1)_Y$, as the electric charge does, but it is denoted with Y. Therefore, the electroweak force is described by the symmetry group

$$SU(2)_L \otimes U(1)_Y, \tag{2.4}$$

where the index L denotes that the weak isospin current J^i_μ couples only to the left

Multiplets			T	T_3
$\begin{pmatrix}\nu_e\\ e\end{pmatrix}_L$	$\begin{pmatrix}\nu_\mu\\ \mu\end{pmatrix}_L$	$\begin{pmatrix}\nu_\tau\\ \tau\end{pmatrix}_L$	1/2	$+1/2$ $-1/2$
e_R	μ_R	τ_R	0	0
$\begin{pmatrix}u\\ d'\end{pmatrix}_L$	$\begin{pmatrix}c\\ s'\end{pmatrix}_L$	$\begin{pmatrix}t\\ b'\end{pmatrix}_L$	1/2	$+1/2$ $-1/2$
u_R	c_R	t_R	0	0
d_R	s_R	b_R	0	0

Table 2.2.: The multiplets of the weak force together with the weak isospin T and the third component T_3 of the weak isospin. The weak eigenstates d', s' and b' result from the CKM-rotation of the mass eigenstates[3].

handed doublets. An isotriplet of vector fields W^i_μ couples to the weak isospin current with a strength g and a single vector field B_μ couples to the weak hypercharge current j^Y_μ, where the strength is assumed to be $g'/2$. This results in an electroweak interaction

$$-ig(J^i)^\mu W^i_\mu - i\frac{g'}{2}(j^Y)^\mu B_\mu. \tag{2.5}$$

The fields $W^\pm_\mu = \sqrt{\frac{1}{2}}(W^1_\mu \mp iW^2_\mu)$ describe the $W^\pm$ Bosons. Other than those two fields the remaining W^3_μ and B_μ are uncharged fields. A linear combination of them results in a massless field

$$A_\mu = B_\mu \cos(\Theta_W) + W^3_\mu \sin(\Theta_W), \tag{2.6}$$

that is the physical state of the photon, and in a massive field

$$Z_\mu = -B_\mu \sin(\Theta_W) + W^3_\mu \cos(\Theta_W), \tag{2.7}$$

that is the physical state of the Z Boson. The mixing angle Θ_W is called the Weinberg angle, defined via the relation

$$\cos(\Theta_W) = \frac{m_W}{m_Z} \approx 0.88. \tag{2.8}$$

The masses of the $W^\pm$ and Z Bosons are the result of spontaneous symmetry breaking via the Higgs Mechanism [4].

2.2. The Top Quark

The top quark was discovered in 1995 at FERMILAB by the detectors CDF [5] and DØ [6] at a center of mass energy (CME) $\sqrt{s} = 1.8\,\text{TeV}$. Its huge mass results in a coupling to the Higgs field in the order of unity, what raises the question if the top quark plays a special role in symmetry breaking.

2.2.1. Top Quark Properties

The top quark is a third generation quark and the isospin partner of the bottom quark. It has charge $Q = +\frac{2}{3}\text{e}$ and spin $s = \frac{1}{2}$. In 2014 the CDF and DØ Collaborations published a combined value of the top quark mass [7]:

$$m_t = 174.34 \pm 0.37(\text{stat.}) \pm 0.52(\text{syst.})\,\text{GeV}. \tag{2.9}$$

The total uncertainty can be calculated as the squared sum of the statistical and the systematic uncertainty and results to $\sigma_{m_t} = 0.64\,\text{GeV}$, which corresponds to a relative uncertainty of $\frac{\sigma_{m_t}}{m_t} = 0.37\%$.

Because of its huge mass, the top quark is the only quark able to decay into a real W boson and another quark. The produced quark is in nearly every case a bottom quark since the corresponding element $|V_{tb}|^2$ of the CKM-matrix is nearly unity. Its huge is the reason for its extremely short lifetime $\tau \approx 0.5 \cdot 10^{-24}\,\text{s}$, which is especially shorter than the time quarks need to hadronise. Thus, the top quark decays before it hadronises, so that its properties are directly accessible.

The decay width, defined as the reciprocal lifetime, is predicted in the SM at next-to-leading-order as:

$$\Gamma_t = \frac{G_f m_t^3}{8\pi\sqrt{2}} \left(1 - \frac{M_W^2}{m_t^2}\right)^2 \left(1 + 2\frac{M_W^2}{m_t^2}\right) \left[1 - \frac{2\alpha_S}{3\pi}\left(\frac{2\pi^2}{3} - \frac{5}{2}\right)\right], \tag{2.10}$$

where G_f is the Fermi coupling constant and α_S the coupling constant of the strong force, with $\alpha_S(M_Z) = 0.118$ [8]. The decay width is also defined as the width of the mass Breit-Wigner distribution at half of the maximum height. A previous indirect measurement of the top quark decay width at CMS [9] achieved a result of

$$\Gamma_t = 1.36^{+0.14}_{-0.11}\,\text{GeV}. \tag{2.11}$$

However, this result is model dependent as it uses the SM single top quark production cross-section and the coupling between the W boson and the top and bottom quark as

input. A direct measurement on the other hand is model independent, but has higher uncertainties. The previous measurement at CDF [5] achieved the result

$$1.10\,\text{GeV} < \Gamma_t < 4.05\,\text{GeV} \tag{2.12}$$

at 68% confidence level, using the CDF Run II data set.

2.2.2. Top Quark Production

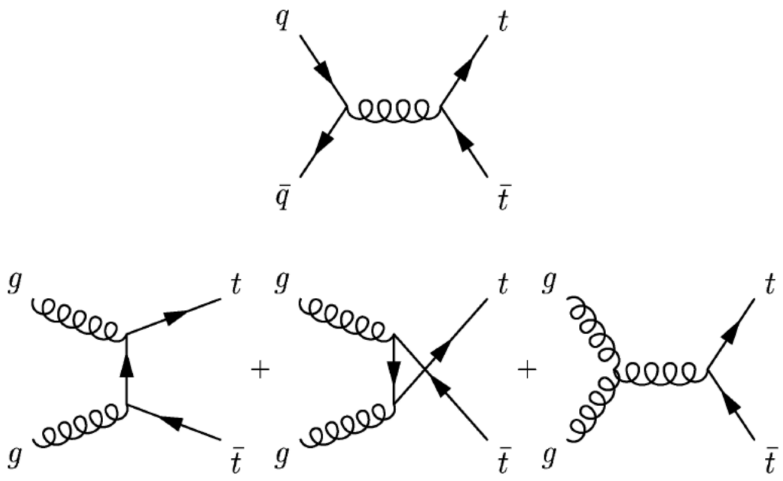

Figure 2.2.: Two different ways of producing top quark pairs in their leading order Feynman diagrams. In the upper row a $q\bar{q}$ fusion is shown, in the lower row the three different channels of gluon fusion.

The production of top quarks is possible either as a $t\bar{t}$ pair or as a single top quark. In hadron colliders, top quark pairs are produced through gluon and $q\bar{q}$ fusion, whose leading order Feynman diagrams are shown in Fig. 2.2. Because of the collision being inelastic, the partons of each hadron interact. Each parton has only a fraction of the momentum of the hadron, which is described by the Bjorken scaling variable x, or just Bjorken x. The parton distribution function depends on x and the momentum transfer Q^2. A plot is shown in Fig. 2.3. The effective center of mass energy of two partons 1 and 2 can be calculated as $\sqrt{\hat{s}} = \sqrt{x_1 x_2 s}$. To produce a pair of top quarks, the effective CME is constrained as follows:

$$\sqrt{\hat{s}} \geq 2m_t. \tag{2.13}$$

Assuming both partons have approximately equal fractions of the total momentum of the hadron, we get

$$x \geq \frac{2m_t}{\sqrt{s}}. \tag{2.14}$$

As the TEVATRON had an energy of $\sqrt{s} = 1.96$ TeV a minimum of $x = 17.7\%$ is needed, thus the majority of all produced top quark pairs is produced via $q\bar{q}$ fusion. The minimum x for the LHC is computed to be $x = 4.3\%$ at $\sqrt{s} = 8$ TeV and $x = 2.7\%$ at $\sqrt{s} = 13$ TeV. Therefore most top quark pairs are produced through gluon fusion. The total cross-sections for $t\bar{t}$ pairs are given in Tab. 2.3.

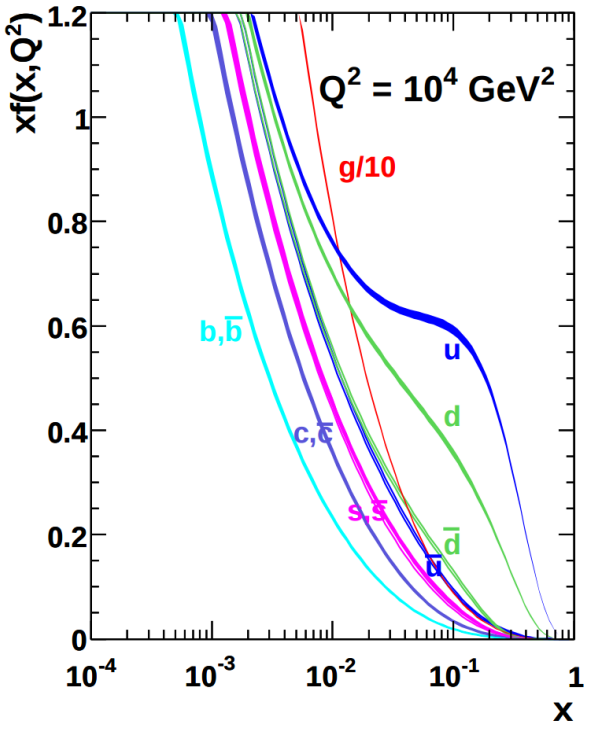

Figure 2.3.: The Parton Distribution Function (MSTW 2008) for a momentum transfer of $Q^2 = 10^4$ GeV [10].

$\sqrt{s}$ [TeV]	7	8	13
$\sigma_{t\bar{t}}$ [pb]	$173.6^{+4.5\ +8.9}_{-5.9\ -8.9}$	$247.7^{+6.3\ +11.5}_{-8.5\ -11.5}$	$816.0^{+19.4\ +34.4}_{-28.6\ -34.4}$

Table 2.3.: Calculated production cross section of $t\bar{t}$ pairs for three different CMEs of the LHC, calculated at NNLO for $m_t = 173.2\,\text{GeV}$ [11].

Single top quark production is accomplished through the processes $q\bar{q}' \to t\bar{b}$ and $qb \to q't$, which are mediated by an s-channel W boson and a t-channel W boson, respectively. Another process that produces a single top quark is $gb \to tW^-$ which involves gluons g. All three processes are shown in their first order Feynman diagrams in Fig. 2.4. The cross-sections of the single top quark productions are proportional to the element $|V_{tb}|$ of the CKM-matrix, thus they can be used to measure it directly [8].

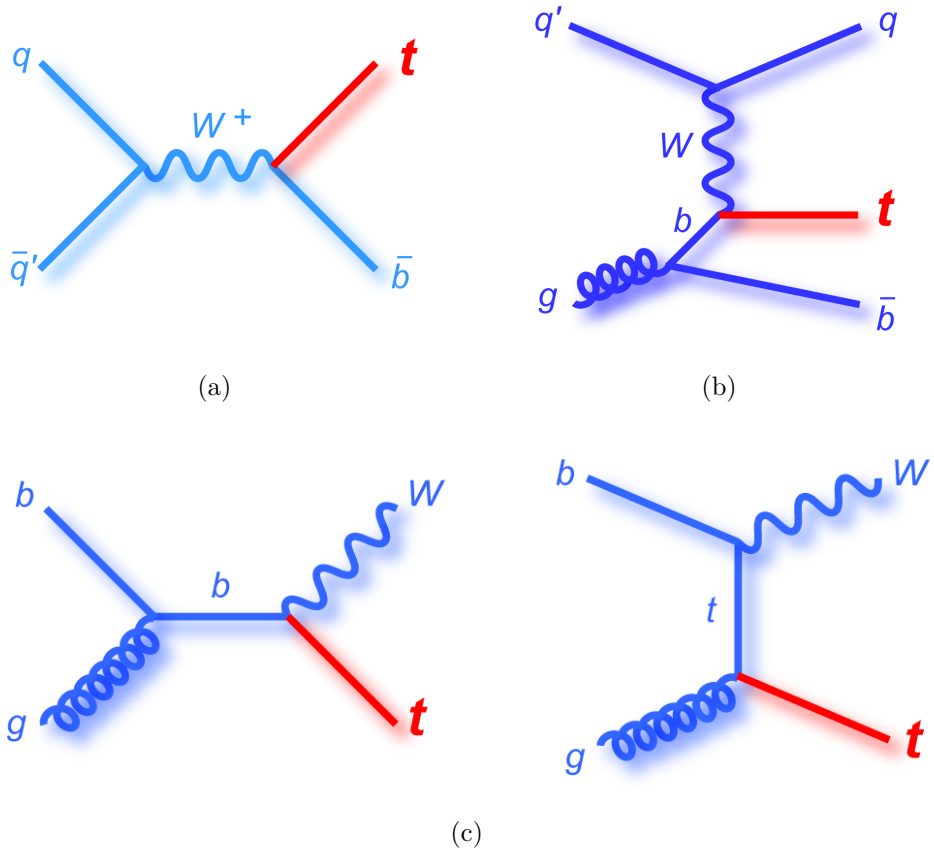

Figure 2.4.: The production of single top quarks via the s-channel (a), the t-channel (b) and with a W boson (c).

2.2.3. Top Quark Decay

The top quark can decay into each down-type quark, via emission of a W boson. Each decay is proportional to the corresponding CKM-matrix element $|V_{ti}|^2$, with $i \in \{d, s, b\}$. The average of many direct single top quark measurements of the element $|V_{tb}|$ is

$$|V_{tb}| = 1.021 \pm 0.032 \tag{2.15}$$

and is therefore approximately equal to one [8]. Thus, the top quark decays to almost 100% into a bottom quark and a W^+ boson, the top antiquark decays into a bottom antiquark and a W^- boson, respectively. The final states are characterised by the decay products of the W boson, which can decay hadronically into a $q\bar{q}'$ pair, with a measured branching ratio of $BR_{\text{had}} = (67.41 \pm 0.27)\%$ [8], or into a charged lepton ℓ and its antineutrino, with a branching ratio of $Br_\ell = (10.86 \pm 0.09)\%$ [8] per lepton. Since the decays of the W bosons are independent of each other, there are three possible decay channels.

- **All jets decay channel**. Both W bosons decay hadronically. The probability of this channel is based on the values above

$$P_{\text{had}} = (BR_{\text{had}})^2 \approx 45.4\%, \tag{2.16}$$

thus it has a statistical advantage, but at the same time it has a large amount of background from QCD multijet processes.

- **Dileptonic decay channel**. Both W bosons decay into a lepton and a neutrino. Since the signature of the τ lepton is similar to hadrons, this channel considers only electrons and muons as leptons. Therefore, the probability of this channel is based on the values above

$$P_{\text{dil}} = (2BR_{\ell})^2 \approx 4.7\%. \tag{2.17}$$

The signature is the cleanest of all three decay channels, but the statistics are low. Another problem are the neutrinos that can not be detected. They can only be reconstructed through the missing transverse energy $\not{E}_T$ as a superposition, not as separate particles.

- **Lepton + jets decay channel**. In the lepton + jets decay channel one W boson decays hadronically, the other leptonically. As in the dileptonic decay channel, only electrons and muons are considered as leptons. The resulting probability is based on the values above

$$P_{\ell + \ jets} = 4BR_{\text{had}}BR_{\ell} \approx 29.3\%. \tag{2.18}$$

The lepton + jets decay channel has a clearer signature than the hadronic decay channel and higher statistics than the dileptonic decay channel. Also the neutrino can be reconstructed through a measurement of the $\not{E}_T$. Therefore, this channel will be used for the measurement of the top quark decay width. An example for the lepton + jets decay channel is shown in Fig. 2.5.

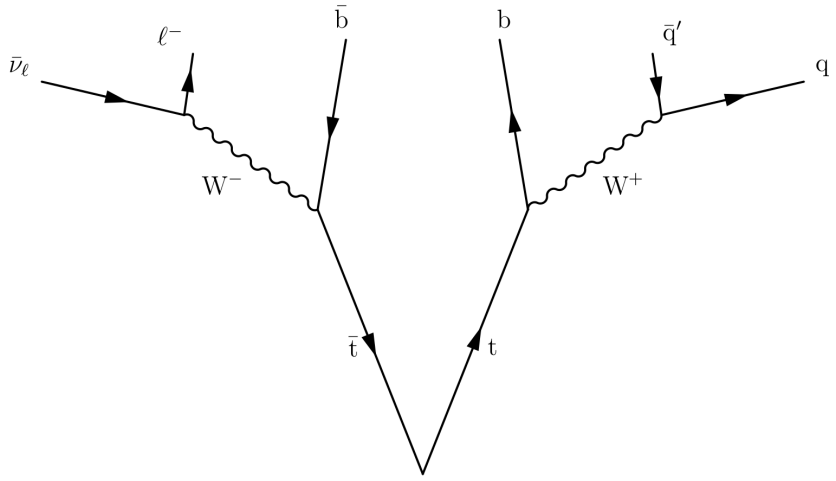

Figure 2.5.: An example of the lepton + jets decay channel. In the shown process the W^- decays leptonically and the W^+ hadronically.

3. Experimental Setup

The measurement of the top quark decay width is conducted at the ATLAS detector at the accelerator LHC (**L**arge **H**adron **C**ollider) of the European Organization for Nuclear Research CERN (**C**onseil **E**uropéen pour la **R**echerche **N**ucléaire) in Geneva. This chapter will introduce the LHC and the ATLAS detector.

3.1. The LHC

The LHC is an approximately 27 km long circular particle accelerator built under the surface near Geneva, that is used for proton-proton collisions as well as heavy ion collisions, predominantly lead ions. It is designed to reach a CME of $\sqrt{s} = 14\,\text{TeV}$ and a luminosity of $\mathcal{L} = 10^{34}\,\text{cm}^{-2}\text{s}^{-1}$. A single beam of protons consists of 2808 bunches, with 1.1×10^{11} protons each. It uses superconducting magnets at a temperature of 1.9 K to control the beam. There are a total of 9593 magnets, that reach a peak magnetic dipole field of 8.33 T. The data used in the analysis was collected at a CME of $\sqrt{s} = 8\,\text{TeV}$ in the year 2012. Previously the LHC ran at a CME of 7 TeV starting 2010. Since 2015 it runs at a CME of 13 TeV.

There are 8 insertion points that can be used for experiments like ATLAS, for beam injections, for the beam dump or for beam cleaning with collimators. Beside ATLAS currently 5 other experiments are in use, those are ALICE (**A** **L**arge **I**on **C**ollider **E**xperiment), CMS (**C**ompact **M**uon **S**olenoid), LHCb (**L**arge **H**adron **C**ollider **B**eauty) and two smaller experiments. The part of the LHC between two insertion points are called sections. Each section has an independent powering. Fig. 3.1 shows the different sections and insertion points and the way they are used.

If the beam becomes unstable, it gets extracted from the collider into the beam dump. Another protection mechanism are the collimators. Collimators are movable metal plates out of graphite or tungsten. They can absorb the particles, so that the unstable beam can not damage other equipment of the collider.

Before the beam gets injected into the LHC, the protons get accelerated in other particle accelerators. The PS Booster accelerates them up to 1.4 GeV. Afterwards, the PS

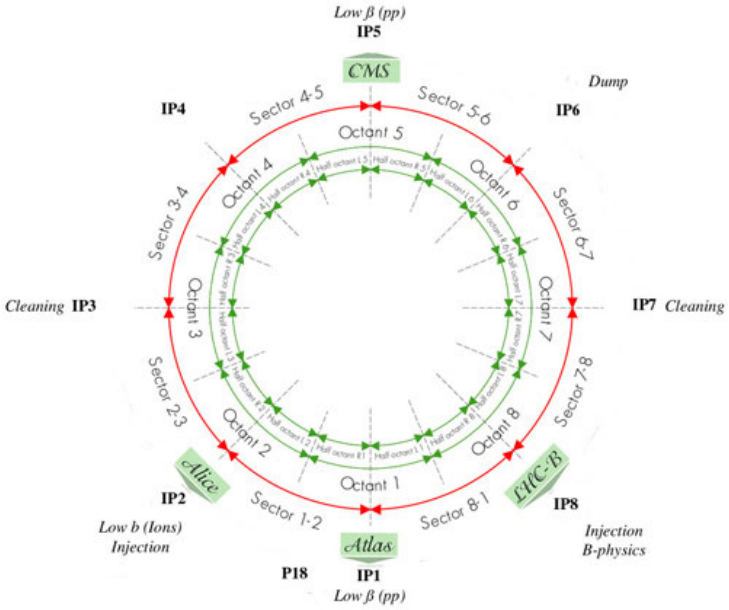

Figure 3.1.: Shown are the insertion points (IP) and the resulting division into sectors. With exception of IP4, all insertion points are currently used, for the experiments, beam cleaning with collimators or the beam dump.©CERN

accelerates them up to 25 GeV and in the SPS the protons get to an energy of 450 GeV before they are injected into the LHC [12].

3.2. The ATLAS-Experiment

The ATLAS (**A** **T**oroidal **L**HC **A**pparatu**S**) detector is one of the two multi-purpose detectors at LHC, beside CMS, and consists of several individual detectors: an inner detector, calorimeters and muon chambers (see Fig. 3.2). ATLAS measures 44 m in length and 25 m in diameter, while weighing about 7000 t.

3.2.1. Coordinate System and Observables

The interaction point in the beam pipe is defined as the origin of the coordinate system. The z-axis is defined by the beam direction, the x-axis pointing to the centre of the collider and the y-axis points upwards. However, commonly a polar coordinate system is used with the azimuthal angle Φ measured in the x-y plane and Θ being the angle between the

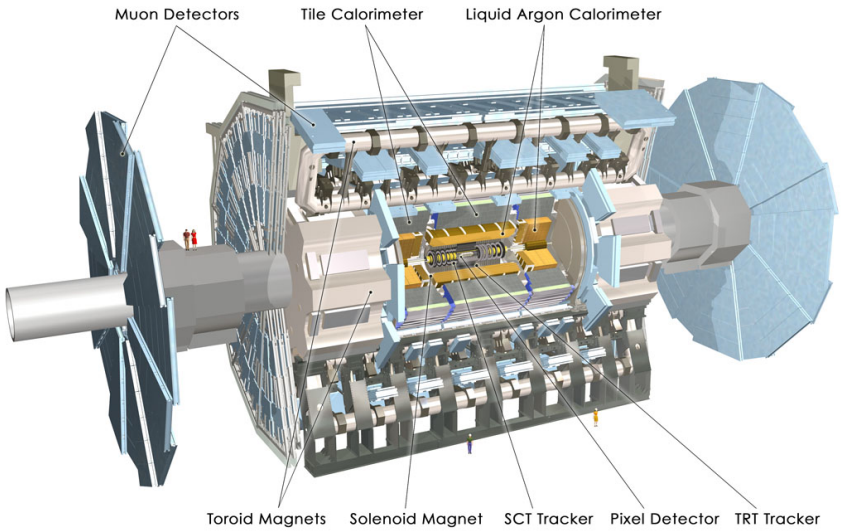

Figure 3.2.: A schematic drawing of the ATLAS detector. Shown are the different parts of the Inner Detector, the Calorimeter, the Muon Spectrometer and the Magnet System.©CERN

momentum of a particle and the z-axis. With Θ, the pseudorapidity can be defined as

$$\eta = -\ln \tan\left(\frac{\Theta}{2}\right). \tag{3.1}$$

It is very useful, because differences $\Delta\eta$ are Lorentz invariant. The name comes from its relation to the rapidity

$$y = \frac{1}{2}\left(\frac{E + p_z}{E - p_z}\right), \tag{3.2}$$

that is used for massive objects, like jets. The pseudorapidity equals the rapidity if the energy $E \gg m$. In addition to that, the distance

$$\Delta R = \sqrt{\Delta\eta^2 + \Delta\Phi^2} \tag{3.3}$$

is defined, with differences $\Delta\eta$ and $\Delta\Phi$ between two particles [13]. This relation will be used during the event reconstruction.

3.2.2. The Detector Components

The magnetic system of ATLAS took about 15 years to get operational and consists of one solenoid magnet and three toroid magnets. The solenoid magnet has a total diameter of 2.56 m and a length of 5.8 m. It is located between the inner detector and the calorimeters.

In consideration of the functionality of the calorimeters, the material thickness was kept as low as possible and is now contributing with approximately 0.66 radiation lengths. It provides a magnetic field of about 2 T for the inner detector.

The three toroid magnets are two end-cap toroids and one barrel toroid. The barrel toroid has an inner diameter of 9.4 m, an outer diameter of 20.1 m and a length of 25.3 m. It creates a magnetic field for the central muon detectors with a strength of approximately 0.5 T. The end-cap toroids exhibit an inner diameter and outer diameter of 1.65 m and 10.7 m, respectively, and a length of 5 m. They create a field of about 1 T for the end-cap muon detectors.

The inner detector is purposed to measure the momentum of all particles and the primary as well as the secondary vertex. The tracks measured need to have a minimum transverse momentum and a pseudorapidity of $|\eta| < 2.5$. The inner detector consists of three sub-detectors. In the inner part of the detector are silicon pixel layers, using discrete space points, and silicon microstrip layers. At the outer area of the inner detector is the transition radiation tracker, using several layers of gaseous straw tube elements and radiation material within.

The calorimeter consists mainly out of a liquid argon (LAr) electromagnetic calorimeter and a hadronic calorimeter, consisting of several parts itself. Both are sampling calorimeters, which consist of one material to produce the particle showers and another material, the sampling material, to measure the deposited energy. The electromagnetic calorimeter is divided into a barrel part and end-cap components, that can cover ranges of $|\eta| < 1.475$ and $1.375 < |\eta| < 3.2$, respectively. The hadronic calorimeter contains a tile calorimeter, a LAr forward calorimeter and a LAr hadronic end-cap calorimeter, covering a total range of $|\eta| < 4.9$.

Muons cannot be detected in the other detectors, since they are minimal ionising particles. To detect them overall four different muon chambers are used, the monitored drift tubes, cathode strip chambers, resistive plate chambers and thin gap chambers covering a total range of $|\eta| < 2.7$.

The high design luminosity results in an interaction rate of about 1 GHz, while the readout is limited to about 200 Hz. To reduce the data, a three level trigger system is installed. Each level reduces the amount of collected data significantly by sorting the events that most likely will not produce interesting results out [13].

4. Tools/Framework

The whole analysis is based on scripts using the ROOT [14] framework and the intrinsic library RooFit [15]. At first, general information about ROOT is listed.

ROOT is an object-orientated framework for data analyses on large scales, based on the programming language $C++$. It contains powerful statistical analysis tools, for example, fitting and multidimensional histogramming and tools for visualisation. The development of ROOT was motivated because new colliders produced more data than the older systems based on the programming language Fortran could handle. ROOT offers many classes for different purposes, for example, histograms in different dimensions with variable or fixed bins, that can contain integer or float numbers. The output files have a special format and are called ROOT files with the ending ".root".

4.1. Event Selection

For the event selection, the AnalysisTop framework in version 1.12.0 is used. AnalysisTop is a framework based on ROOT that uses $C++$ code and python scripts to run the code. From here on the term lepton will always refer to charged leptons except tauons. The signature of the $\ell + jets$ decay channel are 4 jets, with 2 of them originating from a b quark, 1 charged lepton and a missing transverse energy $\not{E}_T$, caused by the neutrino. To reduce the influence of background events, additional cuts and specific selection criteria are defined. The events need to contain at least 4 jets, with a transverse momentum of at least $p_T \geq 25\,\text{GeV}$ and a pseudorapidity of $|\eta| \leq 2.5$. Jets with $p_T \leq 50\,\text{GeV}$ need a jet vertex fraction of $|\text{JVF}| \geq 0.5$ in addition. The JVF is a criterion for the probability of one jet belonging to a particular vertex. The detected lepton has to be isolated, meaning a distance $\Delta R \geq 0.4$ to any other reconstructed object of this event. For the definition of ΔR see Ch.3.2.1. Further, the detected lepton has to be the only detected lepton. Because of the comparable high lifetime of bottom quarks, jets originating from such quarks can be identified through special algorithms. This procedure is called b-tagging. Furthermore, there are requirements for the missing energy: $\not{E}_T \geq 40\,\text{GeV}$ or $\not{E}_T \geq 20\,\text{GeV}$ for events with no b-tagged jets or 1 b-tagged jet. Additionally the relation $\not{E}_T + m_W^T \geq 60\,\text{GeV}$ has

to hold for events with no b-tagged jets, as well as for 1 b-tagged jet. For b-tagging, the MV1-tagger [16] is used with an efficiency of $\varepsilon_b = 70\,\%$.

For the simulation of the events, the data is split into the signal and five different backgrounds, see Tab. 4.2. However, the W + jets background can be split into three different parts itself, namely a part considering only the events with the associated production of heavy or light quarks, respectively, and a part considering only events with the associated production of a single c quark. In Tab. 4.2 the different distributions and the corresponding Monte Carlo generators are listed. The quantum chromodynamics (QCD) background is simulated using a data-driven matrix method [17].

Signal	
Events	MC Generator
$t\bar{t}$	POWHEG [18]+PYTHIA [19]
Background	
Events	MC Generator
W + jets	ALPGEN [20]+PYTHIA
Z + jets	ALPGEN +PYTHIA
Diboson	SHERPA [21]
Single top	POWHEG +PYTHIA
QCD	-

Table 4.2.: The different parts of the data distribution and the corresponding MC generator, split into signal and background processes. The QCD background is generated with a data-driven matrix method.

Using the PlotFactory package, developed and internally used for data analyses within the Göttingen Top Group, control plots are created to compare the simulated data with the measured data, see Fig. 4.1 for two examples, created for the top quark mass.

4.2. Event Reconstruction

The event reconstruction is accomplished with the KLFitter [22], also developed in Göttingen. The KLFitter framework is a likelihood-based reconstruction algorithm, that can be applied to any event topologies and models. During the fit a likelihood, consisting of Breit-Wigner functions B and transfer functions W, for each possible assignment of the

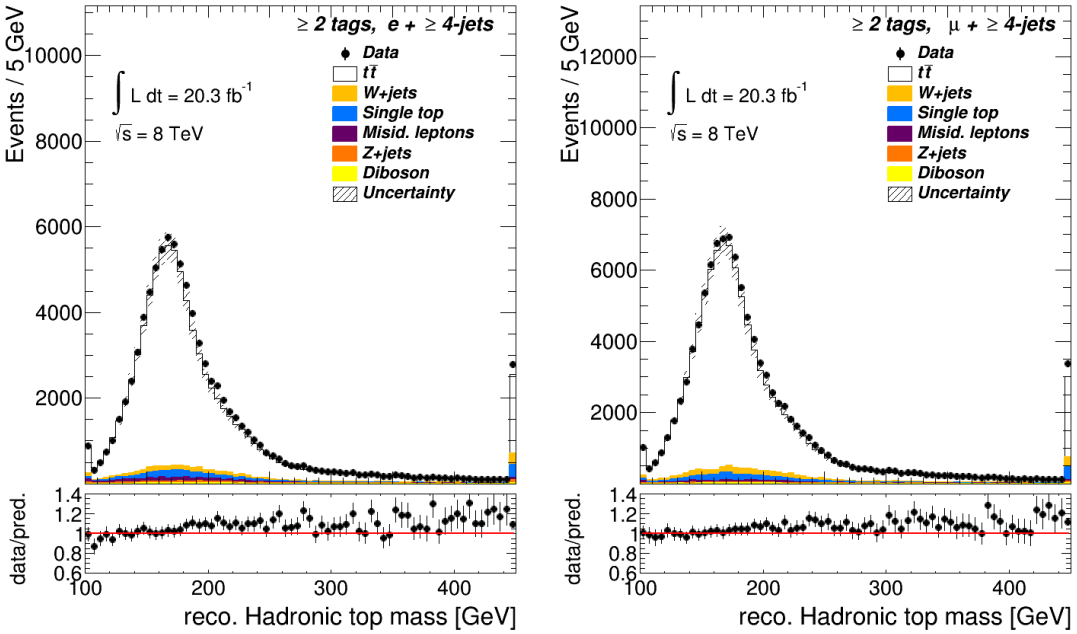

(a) (b)

Figure 4.1.: The added up histograms for the simulated signal and background processes in comparison with the measured distribution. Only events with 2 or more b-tagged jets and an overall of at least 4 jets are considered. Shown is the distribution of the reconstructed top quark mass for (a) electrons and (b) muons. The MC samples agree with the measured data.

jets to their origin vertex is maximised. The likelihood $\mathcal{L}$ can be written as follows:

$$\begin{aligned}\mathcal{L} =& B(m_{q_1q_2q_3}|m_t,\Gamma_t)\cdot B(m_{q_1q_2}|m_W,\Gamma_W)\cdot B(m_{q_4\ell\nu}|m_t,\Gamma_t)\cdot B(m_{\ell\nu}|m_t,\Gamma_t)\\ &\cdot\prod_{i=1}^{4} W_{jet}(E_i^{meas}|E_i)\cdot W_\ell(E_\ell^{meas}|E_\ell)\cdot W_{miss}(\not{E}_x|p_x^\nu)\cdot W_{miss}(\not{E}_y|p_y^\nu),\end{aligned} \tag{4.1}$$

with the top quark mass m_t, the invariant masses m_{xyz}, calculated from the measured particles' x,y and z four-momenta, the decay widths Γ_x, the jet energies E_i and the charged lepton energy E_ℓ. The KLFitter [22] can use different options, specifying the number of jets that shall be considered in the fit.

The option used in my analysis is abbreviated as 5jOPT in the following. This option considers an additional b-tag weight. The two jets with the highest b-tag weight and the remaining three jets with the highest p_T are permuted between the four vertices emitting jets.

In the next step, pseudo-data will be fitted to the measured data distribution using a template method. This is described in detail in the next chapter.

5. The Measurement of the Top Quark Decay Width

This chapter shall provide basic information about the way of measuring the top quark decay width using a template method. Furthermore, the most important uncertainties affecting the result are listed and explained, including the studied initial and final state radiation. At last, the choice of the observables under study will be explained. In the beginning, a brief introduction to RooFit will be provided, which will be used for the fit implementation.

For the process of fitting, a ROOT library, named RooFit [15], containing $C++$ classes is used. It has been originally released as RooFitTools in the BaBar Collaboration in the year 1999. RooFit represents variables, integrals and functions, such as probability density functions, as $C++$ objects. Aside from that, RooFit can be used for plotting and conducting pseudo-experiments, via Monte Carlo generation. RooFit can use a binned or unbinned maximum likelihood fit and a χ^2 fit.

5.1. Template Method

To measure the decay width Γ_t, a template method is used, where simulated distributions for different values of Γ are compared with a measured or generated distribution of one observable. The distribution which fits best to the nominal distribution will be used to determine the true value of Γ in an interpolation. In this analysis, 55 different values are considered, reaching from 0.01 GeV to 8 GeV, mostly in steps of 0.1 GeV. The fit procedure will now be explained in detail.

At first, the produced distributions for signal and background, whose production is described in the previous Ch. 4, are converted into RooFit objects that treats them like probability distribution functions (PDF). All the different distributions are evaluated, as well as a combined distribution. The distributions for just the signal and for the signal combined with the background are shown as an example for the top quark mass in Fig. 5.1. The "RooHistPDF" class treats histograms as PDFs. While for the background

distributions only one RooFit PDF object is created, because of its independence from the width, for the signal and the combined data PDF objects are generated for every available width. Those RooFit PDF objects are the input for the code, executing the template fit.

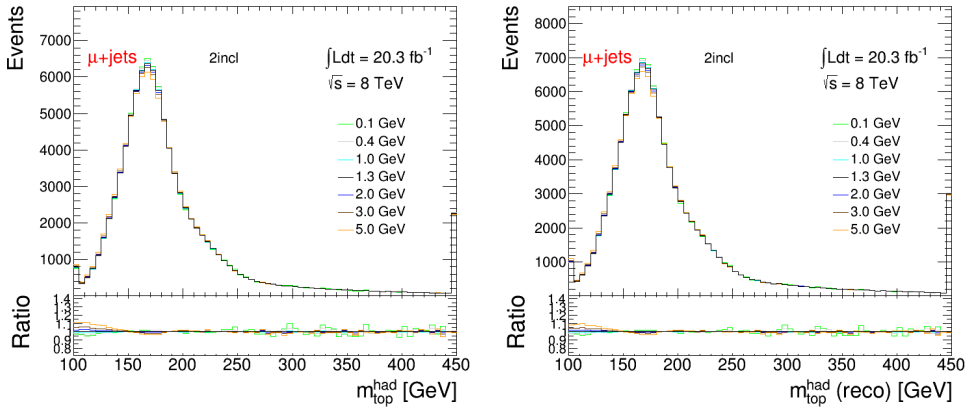

(a) (b)

Figure 5.1.: Different distributions of the top quark mass reconstructed through the hadronic decay branch. The emitted lepton is a muon, the decay has at least 2 b-tagged jets and the KLFitter option is 5jOPT. Each distribution is plotted for 7 different values of Γ listed in the plot. Those distributions are the templates used in the fit. (a) The distribution of the signal. (b) The distribution of the signal combined with the background.

5.1.1. Fit Code

The fit code uses the defined histograms to create pseudo-data, also called toy data. To do so, commands of the RooFit library described above are used, that were developed for this purpose. In the first step, the histogram for a decay width $\Gamma_0 = 1.33\,\text{GeV}$ for signal, as well as background contributions are extracted. For a cross-check and a later normalisation, the total event numbers for each process are extracted. Those event numbers are printed to hint at an error in the previous steps of the analysis, if the number of combined events does not equal the sum of the number of all processes. The same is done for the decay width Γ_x that is given to the fit code as an input and represents the width considered to be the real decay width. If the fit works properly, this width will be the result of the fit, too.

After that, the fit starts and is performed a number of times, specified in the input. Usually 1000 pseudo-experiments are performed in the analysis. For each toy experiment, a histogram will be created for the signal and the combined distribution, via fluctuating

the content of the bins in the nominal histogram, according to Poisson statistics. The number of background events will be fluctuated, too, for each background process. The fluctuation is Gaussian with a mean of the computed number of events of the specific background process and a width of specific fractions of the mean. This accounts for the additional Gaussian constraint on the background distributions, see below. The pseudo-data generated in this way, will be used as input to the fit.

For each width Γ_x, a likelihood is defined as

$$\mathcal{L}(< \text{obs.} > |\Gamma_x) = \sum_{\text{Sig.+BKG}} PDF_x(< \text{obs.} > |\Gamma_x) \prod_{\text{BKG}} PDF(\text{Gauss}), \tag{5.1}$$

where PDF corresponds to the RooFit PDF objects defined above and Gaussian priors to constrain the background distributions. This likelihood is maximised, or the negative logarithmic likelihood (nLL) is minimised. The RooFit commands used for the fit are based on MINUIT [23]. For each width the minimum negative logarithmic likelihood (nLL), the highest likelihood, will be saved.

After that, the minimum nLL and the nLL of the neighbouring widths are approximated as a function of the width using a second degree polynomial. The input points are denoted as (x_l,y_l) for the lower width and the corresponding nLL, (x_0,y_0) for the medium width and (x_h,y_h) for the higher width. For the interpolation the form

$$y(x) = (\mathrm{d}_2 y)(x - x_0)^2 + (\mathrm{d}_1 y)(x - x_0) \tag{5.2}$$

is used, with $(\mathrm{d}_i y)$ being the i-th derivation of y at x_0. The second derivative is approximated by

$$\mathrm{d}_2 y = 2\frac{(y_h - y_l)/(x_h - x_0) - (y_l - y_0)/(x_l - x_0)}{x_h - x_l}. \tag{5.3}$$

The sign of it is determining the value x_m, that minimises the nLL. This is the result of the fit.

In the end, the uncertainty of the result and the pull value is calculated. The uncertainty is calculated by an quadratic fit to the nLL values. If the minimum nLL is set to zero, the uncertainty is defined as half the width of the quadratic fit at height one.

The pull is defined as

$$\frac{\Gamma_{fit} - \Gamma_0}{\sigma_\Gamma}. \tag{5.4}$$

The distribution resulting from many calculated pulls, should be a Gaussian with a mean of 0 and a width of 1, due to the central limit theorem. It can be used to validate the functionality of the fit code. Deviations from the expectation values hint at over- or

underestimation of the uncertainties.

5.2. Uncertainties

The measurement of the top quark width is affected by many systematic uncertainties. Although it is the purpose of this thesis to study the possibilities to reduce the uncertainty caused by initial- and final state radiation (ISR and FSR), the most important systematic uncertainties will be listed and briefly explained in the following for the sake of completeness and for a comparison with the radiation uncertainty. The uncertainties arising from each source listed below are compared in Tab. 5.2. Because of the radiation causing the largest uncertainty, it is justified to focus on this systematic in this thesis.

- **Jet Energy Scale**. The jet energy scale (JES) is the factor, that has to be applied to a measured jet energy on average to correct its value. It can for example be caused through particles within the jet, that do not deposit all of their energy in the calorimeter. The JES is evaluated using well known processes, whose results are compared to the results predicted by simulations. The offset between both results is the JES, that is used to calibrate the detector. The JES uncertainty consists of overall 21 different parts, dependent on p_T and η, originating from the simulation, the calorimeter and the calibration method. For further information see [24]. It is expected to be the dominant and most relevant uncertainty for this analysis.

- **B-tag Scale Factor**. Due to differences between the sample for b-jets and the sample for general jets, an additional scale factor (SF) for correcting the energy of b-jets has to be applied. The uncertainty arising from the b-tag scale factor depends on p_T and η, like the JES uncertainty, see [25].

- **Jet Energy Resolution**. The jet energy resolution (JER) is a measure for the precision of the measurement of the jet energy, that can be achieved with the calorimeter. Many measurements of the same jet energy would result in a Gaussian distribution, due to uncertainties, with a width corresponding to the resolution.

- **Underlying Events**. The underlying events (UE) include any event in the detector, that is not caused by the primary scattering between a $q\bar{q}$-pair, initiating the interesting event. This includes pile-up, multiple parton interactions and beam remnants. A pile-up happens, if more than one collision occur in a single beam crossing. Multiple parton interactions means that more than one parton of each

proton scatters. Those additional scatterings produce mostly particles with lower p_T than the primary scattering.

- **Colour Reconnection**. Colour reconnection (CR) describes the interaction between coloured particles emerging from multiple parton scattering and beam remnants. Due to the high energy of the LHC, many of those events occur and therefore the colour reconnection makes up a significant part of the total uncertainties.

- **Muon Momentum Resolution**. Analogously to the JER, the measured muon momentum has an uncertainty because of the limited resolution of the muon chambers, corresponding to the width of the Gaussian distribution resulting from many measurements of the muon momentum.

- **Electron Energy Scale**. Like the jet energy, the electron energy can not be measured accurately, due to a constant offset between the measured energy and the real energy.

- **Electron Identification Scale Factors**. The identification scale factors quantify differences in the efficiency of the identification of electrons in data and simulation [26].

- **Trigger Scale Factors**. The Trigger scale factor is defined as the ratio between the efficiency for reconstructing muons in real data and the efficiency for reconstruction of muons in MC generated data [27].

- **Fragmentation**. Fragmentation is the process of colour charged particles causing jets, through creating additional quark-antiquark pairs.

- **Monte Carlo Generator**. Different MC generators can produce different distributions for the processes. To estimate the resulting uncertainty the output of different MC generators are compared.

- **Radiation**. The radiation uncertainty stems from initial- and final state radiation. In the case of ISR the incoming particles emit one or more particles like gluons, changing the energy of particles, while FSR refers to particles emitted in the final state. In Tab. 5.2 it can be seen that this uncertainty is much higher than expected. Hence, the reason needs to be studied and identified.

5.3. Observables

For this analysis, five different observables are tested. This is a first approach and not expected to yield optimal results for the decay width of the top quark. The first observable is the mass of the hadronically reconstructed top quark m_t^{reco}. This one was chosen because its distribution defines the decay width of the top quark, see Ch. 2.2.1. However, it is especially sensitive to the jet energy scale and hence not optimal. The observable D_{32} is introduced as the difference between the invariant mass of the 3 jets of the hadronically decaying top quark, and the invariant mass of the 2 jets, emitted by the hadronically decaying W boson. This corresponds to

$$D_{32} = m_t^{\text{reco}} - m_W^{\text{reco}}. \tag{5.5}$$

It is introduced, because effects in the tails of the m_W^{reco} distribution also affect the tails m_t^{reco} distribution and cancel out in difference, therefore D_{32} is more stable than m_t^{reco}.

The third observable in use is R_{32}. It is defined as the ratio between the invariant masses

$$R_{32} = \frac{m_t^{\text{reco}}}{m_W^{\text{reco}}} \tag{5.6}$$

of the 3 jets and the 2 jets, that were used for D_{32}, too. The purpose for defining a ratio, is to minimise the dependencies from the jet energy scale. Intending to combine both advantages of D_{32} and R_{32} respectively, the observable R_{diff} is defined as

$$R_{\text{diff}} = \frac{m_t^{\text{reco}} - m_W^{\text{reco}}}{\bar{m}_W^{\text{reco}}} = \frac{D_{32}}{\bar{m}_W^{\text{reco}}}, \tag{5.7}$$

using an average value of the reconstructed W mass $\bar{m}_W^{\text{reco}}$. The last observable exploits the leptonically decaying top quark. The observable $m_{\ell b}$ is defined as the invariant mass of the emitted lepton and the b quark. In the following, the index “reco” will be dropped.

Systematics [GeV]	D_{32}	R_{32}	R_{diff}	m_{lb}	m_t
Total	$^{+2.84}_{-2.55}$	$^{+4.06}_{-3.92}$	$^{+2.94}_{-2.63}$	$^{+1.10}_{-1.08}$	$^{+5.22}_{-4.27}$
Radiation	$^{+2.20}_{-2.20}$	$^{+3.55}_{-3.55}$	$^{+2.27}_{-2.27}$	$^{+0.16}_{-0.16}$	$^{+3.86}_{-3.86}$
JES	$^{+1.33}_{-0.98}$	$^{+0.38}_{-0.39}$	$^{+1.43}_{-1.02}$	$^{+0.53}_{-0.54}$	$^{+3.14}_{-1.43}$
JER	$^{+0.84}_{-0.01}$	$^{+1.01}_{-0.05}$	$^{+0.83}_{-0.02}$	$^{+0.30}_{-0.08}$	$^{+1.03}_{-0.02}$
B-tag SFs	$^{+0.51}_{-0.46}$	$^{+0.54}_{-0.45}$	$^{+0.51}_{-0.46}$	$^{+0.56}_{-0.58}$	$^{+0.68}_{-0.57}$
UE	$^{+0.55}_{-0.55}$	$^{+1.23}_{-1.23}$	$^{+0.52}_{-0.52}$	$^{+0.44}_{-0.44}$	$^{+0.58}_{-0.58}$
CR	$^{+0.11}_{-0.11}$	$^{+0.76}_{-0.76}$	$^{+0.12}_{-0.12}$	$^{+0.41}_{-0.41}$	$^{+0.54}_{-0.54}$
μ momentum resolution	$^{+0.01}_{-0.01}$	$^{+0.00}_{-0.00}$	$^{+0.01}_{-0.01}$	$^{+0.03}_{-0.03}$	$^{+0.01}_{-0.01}$
Electron energy scale	$^{+0.02}_{-0.01}$	$^{+0.00}_{-0.02}$	$^{+0.01}_{-0.01}$	$^{+0.02}_{-0.04}$	$^{+0.01}_{-0.01}$
JVF	$^{+0.04}_{-0.03}$	$^{+0.19}_{-0.10}$	$^{+0.03}_{-0.02}$	$^{+0.03}_{-0.04}$	$^{+0.08}_{-0.14}$
Electron ID SFs	$^{+0.17}_{-0.16}$	$^{+0.20}_{-0.15}$	$^{+0.18}_{-0.16}$	$^{+0.19}_{-0.17}$	$^{+0.18}_{-0.16}$
Electron trigger SFs	$^{+0.05}_{-0.04}$	$^{+0.03}_{-0.07}$	$^{+0.05}_{-0.04}$	$^{+0.03}_{-0.03}$	$^{+0.05}_{-0.04}$
μ trigger SFs	$^{+0.12}_{-0.11}$	$^{+0.13}_{-0.10}$	$^{+0.14}_{-0.13}$	$^{+0.12}_{-0.13}$	$^{+0.13}_{-0.12}$
MC generator	$^{+0.24}_{-0.24}$	$^{+0.46}_{-0.46}$	$^{+0.36}_{-0.36}$	$^{+0.28}_{-0.28}$	$^{+0.47}_{-0.47}$
Fragmentation	$^{+0.21}_{-0.21}$	$^{+0.26}_{-0.26}$	$^{+0.23}_{-0.23}$	$^{+0.15}_{-0.15}$	$^{+0.23}_{-0.23}$

Table 5.2.: All systematic uncertainties on Γ, for the five observables used in the analysis, as they are defined in Ch.5.3. For every systematic, two uncertainties are listed, the upper one is the upward uncertainty, the lower one is the downward uncertainty.

6. Results

This chapter will explain the way the radiation uncertainty is studied and the attempts to reduce it, because they are the dominant source of uncertainty. As this is not expected, the reason for this needs to be studied and identified. It will start with a section about the validation of the one dimensional fit code and the treatment of the background contributions related to W+jets events. Then, the choice of observable cuts and cuts on kinematic variables, like the logarithmic likelihood (LL), will be explained. After that, the optimisation of the LL cut, the D_{32} and the R_{32} cut is described. Finally, the result of a fit that combines the electron and muon channel as well as the 1 exclusive and 2 inclusive b-tag bin, will be shown. If not explicitly stated, the 2 inclusive b-tag bin and the 5jOPT KLFitter option will be used.

6.1. Validation of the Fit

To check if the data, which is used as the input for the fit code, is consistent with the data produced by PlotFactory after the event selection and reconstruction, the histogram created by PlotFactory and the histogram produced out of the RooFit PDF objects for signal and background combined are plotted together. The latter histogram is plotted with Poisson-fluctuation disabled. Both histograms should be congruent with each other. Deviations would hint at a problem, e.g. different binnings of the histograms in the PlotFactory and the fit code.

The functionality of the fit code can be validated using calibration curves, which plot the result of the fit, using pseudo-data, against the width, that were used to create the pseudo-data. The slope of the calibration curve should be 1 and the intercept 0, because the fit should on average favour the width, that was used as the input. Further, the pull distributions described in Ch. 5.1.1 and defined in Eq. (5.4) are used. In Fig. 6.1 the calibration curves, the pull curves and the expected uncertainties of D_{32} as example are shown for the muon and electron channel.

The pull curves show a deviation from the expected values for the mean and the width, if the decay width is less than 1 GeV. This can be explained with a restriction made on

the results of the fit. Since negative decay widths cannot be defined, they are not allowed as fit results. In the result, the shape of the distribution is not Gaussian any longer and the mean of the distribution gets slightly shifted to higher widths, than the one used as the input. In consequence, the mean of the pull distribution will be shifted, too (compare Eq. (5.4)). The restriction and the caused shift in the mean is the reason for the slope of the calibration curves being greater than 1 as well. Apart from those shifts, the parameters are in good agreement with the expectation values. The calibration curves, the pull curves and the expected uncertainties for the other observables are shown in Fig. A.2-A.5. The pull curve for m_t justifies the focus on the other observables in this analysis. However, the results for m_t will still be listed in the following.

The fit code offers two options regarding the treatment of the W boson background parts, see Ch. 4.1. The first option (Wsum) is to consider it as the sum of all background processes involving a W boson. The second option (Wsplit) describes this background more precisely, by splitting it into three different parts: one considers only the associated production of a pair of heavy quarks b or c (Wbbcc), on the other hand the second part considers only associated produced light quarks (Wlight) and the third part considers only the associated production of a single charm quark (Wc). This change requires to redefine the uncertainties of the occurring number of background events, related to the different background parts. The Monte Carlo related uncertainty of the Wsum-option was 48% of the expected number of events, while the corresponding uncertainties of the Wbbcc-, Wlight- and Wc-background are 11%, 4% and 27%, respectively [26]. Both options were validated via the explained methods. From now on, all presented results were produced using the Wsplit-option because it offers a more accurate background description.

6.2. Comparison of Nominal Sample with Radiation Up/Down Sample

To reduce the systematic uncertainty caused by radiation, cuts on the observables and variables will be applied. The cuts on the observables will be chosen in a way that parts of the range which are especially sensitive to changes in the amount of radiation will be cut off. To determine those parts, histograms for each observable are created, based on samples that consider a higher or lower rate of radiation. Because all background components and systematics are described with specifically created ROOT files, this can easily be done, by changing the input files for the histogram generation. To produce the radiation-up and -down samples with POWHEG and PYTHIA mainly three changes have to be made. The damping parameter h_{damp} is set to finite values $h_{\mathrm{damp}} = m_t$ and

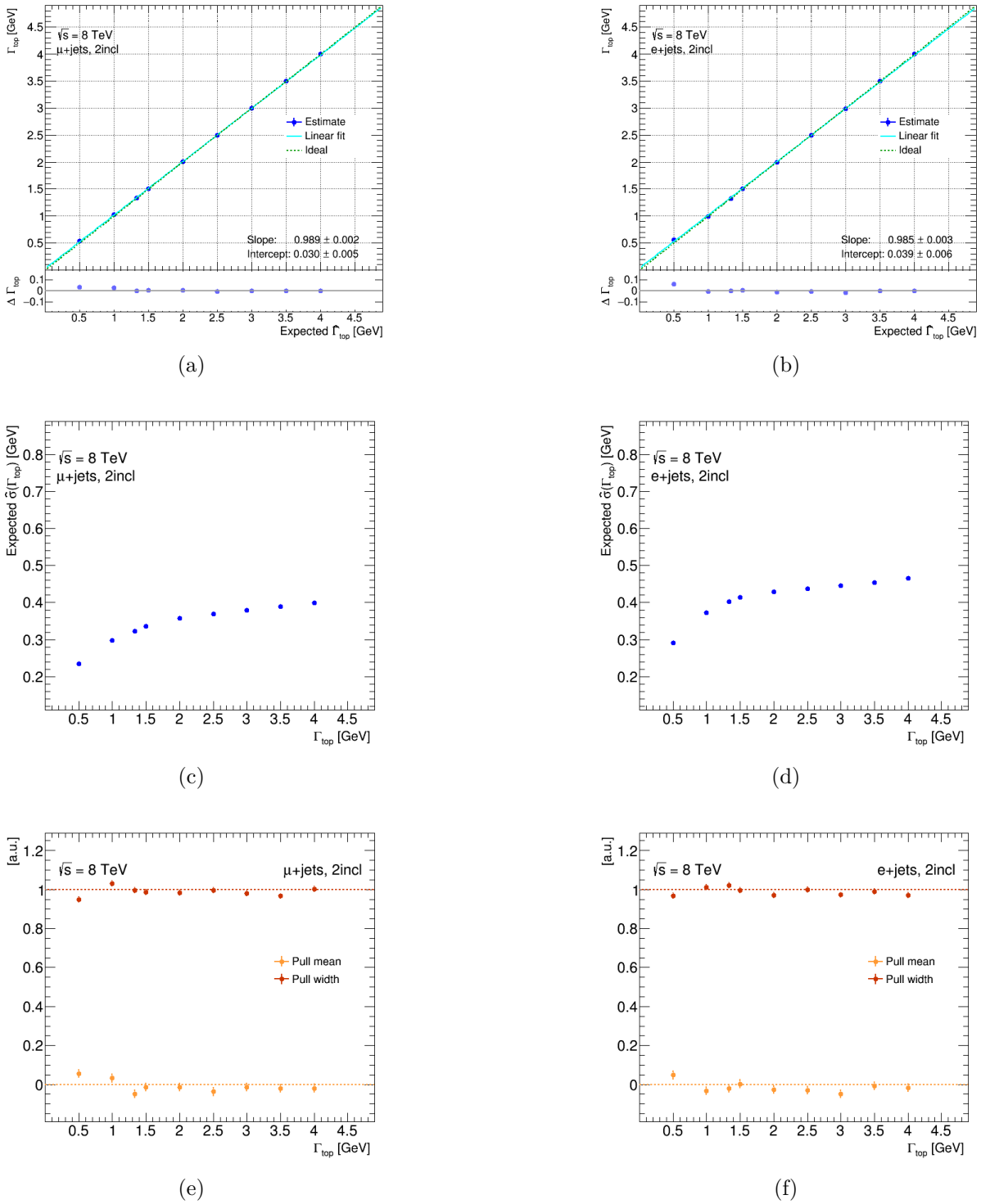

Figure 6.1.: The calibration-, sigma- and pull curves for D_{32} in the muon channel ((a), (c), (e) respectively) and the electron channel ((b), (d), (f) respectively). Both pull curves show a deviation from the expected mean of 0 and width of 1 for decay widths of $\Gamma < 1\,\text{GeV}$. This is caused be the restriction of the results to be non-negative, because a negative decay width can not be defined.

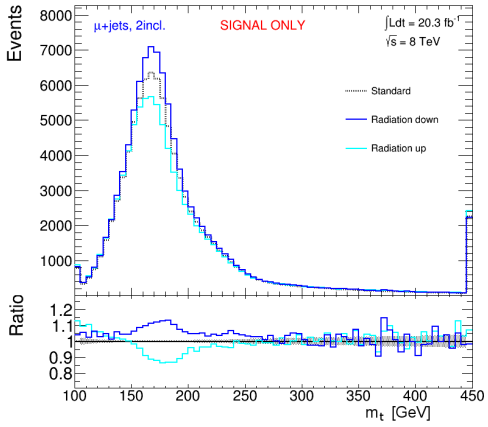

(a)

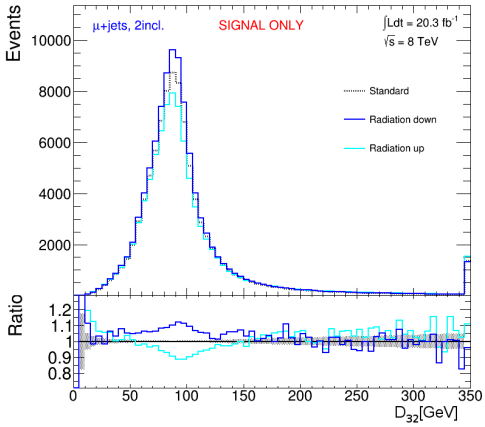

(b)

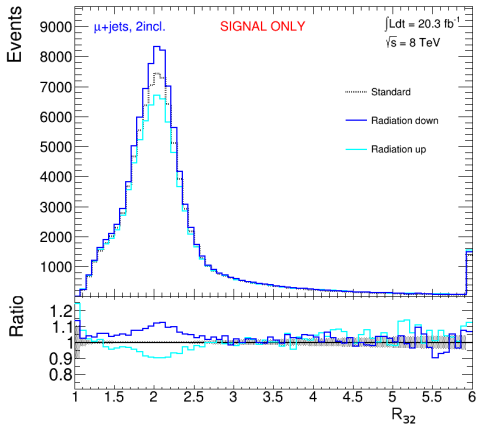

(c)

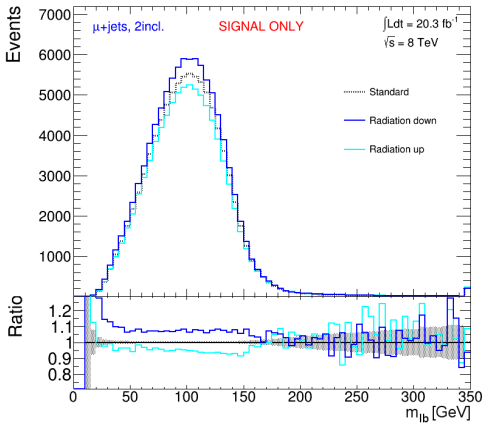

(d)

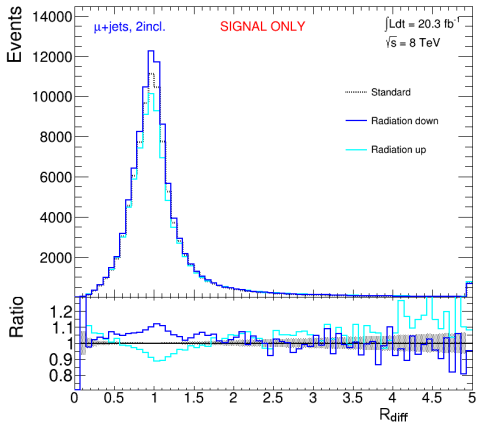

(e)

Figure 6.2.: Comparison of the radiation nominal sample with samples assuming higher or lower radiation, for (a) m_t, (b) D_{32}, (c) R_{32}, (d) $m_{\ell b}$ and (e) R_{diff}. All plots contain only the muon channel.

$h_{\text{damp}} = 2m_t$ for the radiation-down and the radiation-up sample, respectively. Further, the renormalisation scale μ is set to $\mu = 2$ for radiation-down and $\mu = 0.5$ for radiation-up. In addition, the tune is changed to Perugia2012radHi and Perugia2012radLo for radiation-up and radiation-down, respectively [28]. Those histograms are plotted together with the histogram assuming the standard radiation frequency in the muon channel, see Fig. 6.2. For the corresponding plots in the electron channel, see Fig. A.6.

In the tails of all distributions fluctuations of the ratio can be observed. For all distributions aside from $m_{\ell b}$ the ratio peaks at the same point where the distributions peak. On the other hand the ratio is approximately constant in the range of the distribution peak of $m_{\ell b}$. Therefore it is an effect of normalisation.

The cuts are chosen with respect to high relative deviations of the radiation samples from the standard sample, asymmetries and the number of events, that would be cut off. With those aspects in mind, the cuts are chosen and listed in Tab. 6.1. Each set of cuts, also the default range, will be named as "set x", with x being a number. In the following this name will be used to refer to the corresponding set of cuts, because of the large number of cuts, that were made.

6.3. Cuts on Observables

Cuts on the observables have to be implemented in the event selection, the RooFit PDF object generation and the fit code. The changes in the ratio

$$R_{SC} = \frac{\text{number of signal events}}{\text{number of combined events}} \tag{6.1}$$

and the ratio

$$R_{\text{signal}} = \frac{\text{number of signal events with cut}}{\text{number of signal events without cut}} \tag{6.2}$$

are listed in Tab. 6.5. They are considered to control the amount of background events compared to the amount of signal events and to control the amount of signal that is cut off applying a cut.

Thus, the cuts lower the weight of the background events compared to the signal events, while cutting off about 5 to 10 percent of the original signal, aside from $m_{\ell b}$, where the signal is reduced about 2 percent. To calculate the uncertainty arising from the radiation, the fit is conducted using the histograms created based on the radiation-up and -down samples. Regularly, the result for the radiation-up sample will be higher decay widths and for the radiation-down sample lower decay widths. The mean of the distribution of the results where the standard sample was used and the mean of the distribution where

the radiation-up and -down sample, respectively, were used, get subtracted. The larger difference will be considered to be the systematic uncertainty. The statistical uncertainty is already calculated during the fit, see Ch. 5.1.1. To calculate the total uncertainty, both uncertainties are summed up quadratically:

$$\sigma_{\text{total}} = \sqrt{\sigma^2_{\text{syst.}} + \sigma^2_{\text{stat.}}}. \tag{6.3}$$

The results are listed in Tab. 6.3.

Those uncertainties are compared to the uncertainties before applying cuts, see Tab. 6.2. The statistical uncertainties in the muon channel are systematically lower than the one in the electron channel, because of the easier identification of muons. Therefore the number of reconstructed events involving muons is higher.

By comparison of the uncertainties of set 1 and set 2, it can be seen, that no improvements of the radiation uncertainties can be observed. However, the statistical uncertainty could be slightly improved for some observables, also indicated by the better ratio R_{signal}, see Tab. 6.5.

As an attempt to improve the ratios even more, the observables get constrained to an even narrower interval. The new set of cuts (set 3) is shown in Tab. 6.6. The remaining signal in comparison with set 1 and the fraction of the combined events is listed in Tab. 6.7. Between 15 and 30 percent of the signal are cut off while R_{SC} is improved even further.

The uncertainties calculated using this set, see Tab. 6.4, are lower for R_{32} and R_{diff}, but increased for the other observables. But even for the observables for which the uncertainties decreased the radiation uncertainty as well as the statistical uncertainty, is higher than the uncertainties of set 1.

Therefore, it can be concluded that there is neither a correlation between R_{signal} and the radiation uncertainty nor a correlation between R_{SC} and the radiation uncertainty. Apart from that the changes in the uncertainty are individual for each observable, because the distributions of each observable differ significantly, see Fig. 6.2.

A further study of observable cuts will be done in Ch. 6.6.

6.4. Comparison of Kinematic Variables

The cuts on kinematic variables will be chosen the same way, as the cuts on the observables were chosen. The standard radiation sample will be compared with the radiation-up and radiation-down samples. The variables considered for cuts are:

- The transverse momentum of the jets $p_{T,\text{jet}}$

set 1		
Observable	Lower Border	Upper Border
m_t [GeV]	100.0	450.0
D_{32} [GeV]	0.0	350.0
R_{32} [-]	1.0	6.0
$m_{\ell b}$ [GeV]	0.0	350.0
R_{diff} [-]	0.0	5.0

set 2		
Observable	Lower Border	Upper Border
m_t [GeV]	110.0	350.0
D_{32} [GeV]	20.0	180.0
R_{32} [-]	1.0	3.5
$m_{\ell b}$ [GeV]	30.0	200.0
R_{diff} [-]	0.1	2.0

Table 6.1.: The default ranges of the observables on the left and the boundaries of the cuts on the right side, referred to as set 1 and set 2, respectively.

Systematics	m_t	D_{32}	R_{32}	R_{diff}	$m_{\ell b}$
electron					
Radiation [GeV]	±4.33	±2.63	±2.42	±2.57	±0.92
Statistical uncertainty [GeV]	±0.55	±0.42	±0.60	±0.42	±0.57
Total uncertainty [GeV]	±4.36	±2.66	±2.49	±2.60	±1.08
muon					
Radiation [GeV]	±4.35	±2.46	±3.10	±2.04	±1.24
Statistical uncertainty [GeV]	±0.39	±0.35	±0.50	±0.35	±0.49
Total uncertainty [GeV]	±4.37	±2.49	±3.14	±2.07	±1.33

Table 6.2.: The statistical and radiation uncertainties of the fit result for each observable, without cuts.

Systematics	m_t	D_{32}	R_{32}	R_{diff}	$m_{\ell b}$
electron					
Radiation [GeV]	±5.91	±3.23	±3.85	±3.34	±1.33
Statistical uncertainty [GeV]	±0.53	±0.41	±0.60	±0.39	±0.55
Total uncertainty [GeV]	±5.93	±3.25	±3.90	±3.36	±1.44
muon					
Radiation [GeV]	±4.45	±3.23	±3.47	±3.24	±1.41
Statistical uncertainty [GeV]	±0.41	±0.34	±0.49	±0.34	±0.49
Total uncertainty [GeV]	±4.47	±3.25	±3.50	±3.26	±1.49

Table 6.3.: The statistical and radiation uncertainties of the fit result for set 2 and for each observable.

Systematics	m_t	D_{32}	R_{32}	R_{diff}	$m_{\ell b}$
electron					
Radiation [GeV]	±4.55	±3.41	±3.66	±3.31	±1.46
Statistical uncertainty [GeV]	±0.64	±0.49	±0.76	±0.47	±0.82
Total uncertainty [GeV]	±4.60	±3.44	±3.15	±3.34	±1.67
muon					
Radiation [GeV]	±4.36	±3.26	±3.12	±3.02	±1.98
Statistical uncertainty [GeV]	±0.50	±0.36	±0.67	±0.37	±0.73
Total uncertainty [GeV]	±4.39	±3.28	±3.19	±3.04	±2.11

Table 6.4.: The statistical and radiation uncertainties of the fit result for set 3 and for each observable.

Observable	m_t [GeV]	D_{32} [GeV]	R_{32} [-]	$m_{\ell b}$ [GeV]	R_{diff} [-]
electron					
R_{signal} [%]	93.95	93.67	92.62	98.27	93.87
R_{SC} [%] without cut	87.75	87.75	87.75	87.75	87.75
R_{SC} [%] with cut	88.72	88.84	88.75	88.55	88.82
muon					
R_{signal} [%]	93.98	93.67	92.62	98.22	93.86
R_{SC} [%] without cut	89.03	89.03	89.03	89.03	89.03
R_{SC} [%] with cut	89.87	90.04	89.94	89.73	90.01

Table 6.5.: An overview of the changes caused by the cuts of set 2. All cuts improve the fraction of the signal events out of all events.

set 3		
Observable	Lower Border	Upper Border
m_t [GeV]	110.0	200.0
D_{32} [GeV]	40.0	120.0
R_{32} [-]	1.5	2.4
$m_{\ell b}$ [GeV]	50.0	140.0
R_{diff} [-]	0.6	1.4

Table 6.6.: The observable cuts of set 3.

electron		
Observable	R_{signal} [%]	R_{SC} [%]
m_t [GeV]	72.04	90.59
D_{32} [GeV]	80.81	90.09
R_{32} [-]	70.00	90.21
$m_{\ell b}$ [GeV]	84.19	89.97
R_{diff} [-]	78.80	90.41

muon		
Observable	R_{signal} [%]	R_{SC} [%]
m_t [GeV]	71.89	91.72
D_{32} [GeV]	80.75	91.12
R_{32} [-]	69.93	91.22
$m_{\ell b}$ [GeV]	83.69	90.80
R_{diff} [-]	78.72	91.36

Table 6.7.: The Ratios calculated for set 3.

- The transverse mass of the W boson $m_{T,W}$
- The mass of the reconstructed W boson m_W
- The logarithmic likelihood LL
- The missing transverse energy $\not{E}_T$

For the plot of the different samples in the muon channel see Fig. 6.3. The corresponding plots in the electron channel can be found in Fig. A.7. Those five variables were chosen, because they showed the largest deviations and asymmetries and are therefore more promising than other variables.

The cuts on all variables, aside from the transverse W boson mass, are chosen in a way to reduce asymmetries. In addition, a lower border on $m_{T,W}$ is chosen, because of high deviations for low values. The cut on the reconstructed mass of the W boson is more strict than the other cuts because it influences directly the value of all observables that exploit the hadronic branch of the decay. Therefore all values deviating too much from the known value of the mass are cut off. Furthermore, the asymmetries in the ratio of the nominal sample and the radiation samples are considered. The resulting cuts are listed in Tab. 6.8.

6.5. Cuts on Kinematic Variables

The variable cuts are applied together with one set of observable cuts. Observable cuts showed no improvement of the total uncertainty, but they reduced the amount of background in each channel and for all observables. To further reduce the impact of the background on the analysis, the variable cuts are studied in combination with observable cuts. Further, a set with all cuts together should be included to study the interplay of observable and variable cuts. Set 3 has the best ratio R_{SC}, but also less statistics than

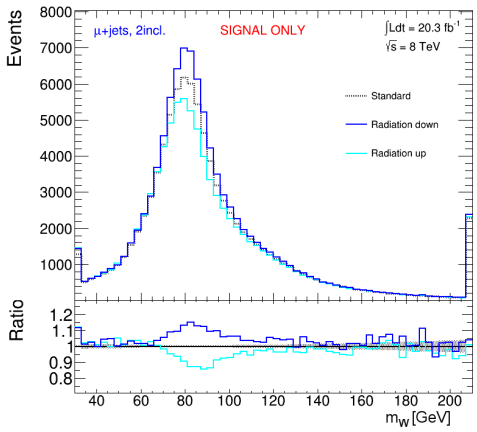

(a)

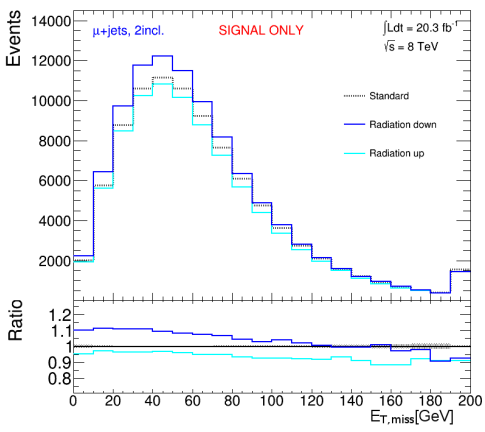

(b)

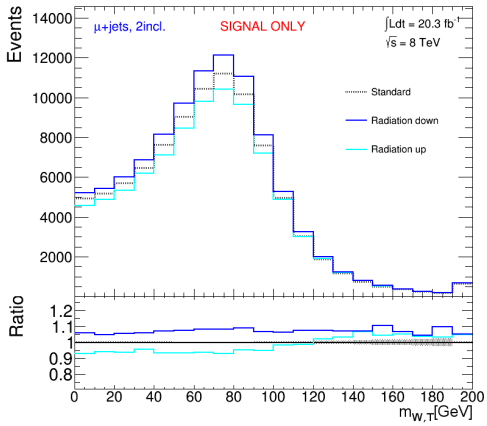

(c)

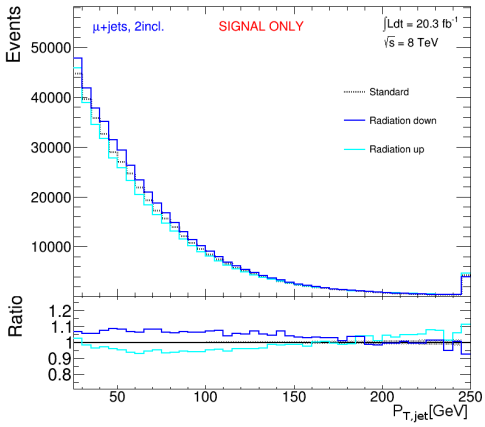

(d)

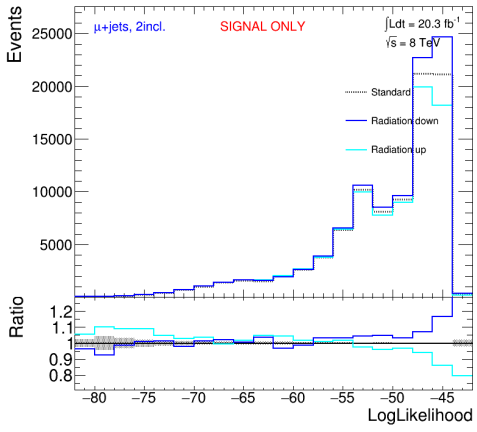

(e)

Figure 6.3.: Comparison of the radiation standard sample with sample assuming higher or lower radiation, for (a) m_W, (b) $\not{E}_T$, (c) $m_{T,W}$, (d) $p_{T,\text{jet}}$ and (e) LL. All plots for the muon channel.

the other sets, which will be decreased even more through the new cuts. Therefore new sets of cuts will be defined using the observable cuts of set 2. The new sets are listed in Tab. 6.9.

The ratios of the sets with a single variable cut are shown in Tab. 6.11. Applying the cut on $p_{T,\text{jet}}$ in set 5 produces the purest data with a ratios $R_{SC} \approx 94\%$ and $R_{SC} \approx 95.5\%$ for the electron- and the muon channel respectively. The greatest toll on the signal is taken by the cut on the W boson mass, which reduces the amount of signal events to approximately 60% of the original amount, for the electron- and muon channel. Aside from the combinations of the cuts that are listed as sets, 8 other combinations were tested. The LL cut was combined with any of the other five variable cuts. Further, it was combined with the cut on $\not{E}_T$ and $p_{T,\text{jet}}$ as one set, and with $\not{E}_T$, $p_{T,\text{jet}}$ and both cuts on $m_{T,W}$ as another set. The latter one was also tried out, without the LL cut.

The cut on the reconstructed W mass in set 9 improves the uncertainties of all observables reconstructed through the hadronic branch of the decay significantly, because of its direct influence on those observables. Set 5 shows good results for $m_{\ell b}$ in both channels. However the lower boundary of $m_{T,W}$ in set 6 showed the best result for $m_{\ell b}$ in the electron channel, and the LL cut showed a result for $m_{\ell b}$ in the muon channel approximately as good as the $p_{T,\text{jet}}$ in set 5. Moreover the LL cut showed good improvements for D_{32} and R_{32} in the muon channel.

However, the best result was achieved with the combined cuts in set 10, see Tab. 6.10. Although the number of events is drastically decreased compared with set 1, the statistical uncertainty improved because of the higher purity of the data of more than 96% for the electron channel and even over 97% in the muon channel. The fit code is not stable for small amount of events, when using the radiation-up sample, that reduces the number of events even more, because many fit results are set to 0. The stability problems are caused by the binning of the histograms. With the current number of bins, many of them contain only a small amount of events. Reducing the number of bins and consequently increase the content of the bins improves the stability of the fit because of a higher statistical significance of each bin. The listed value corresponds to such a setting without 0 GeV results. Values calculated this way serve only as estimators for the order of magnitude of the uncertainty and are labelled with a star. The statistical uncertainty can be calculated anyway because it is independent from the radiation samples. A further refinement of the variable cuts and the observable cuts, as well, will be done in the next chapter.

Variable	Lower Border	Upper Border
m_W [GeV]	60.0	100.0
$\not{E}_T$ [GeV]	0.0	150.0
$m_{T,W}$ [GeV]	20.0	150.0
$p_{T,\text{jet}}$ [GeV]	25.0	140.0
LL [-]	-54	-42

Table 6.8.: Variable cuts chosen by comparing different radiation samples.

Observable	Lower Border	Upper Border
m_t [GeV]	110.0	350.0
D_{32} [GeV]	20.0	180.0
R_{32} [-]	1.0	3.5
$m_{\ell b}$ [GeV]	30.0	200.0
R_{diff} [-]	0.1	2.0

Additional Cuts	Defined Set
LL [-]	set 4
$p_{T,\text{jet}}$ [GeV]	set 5
$m_{T,W}$ lower border [GeV]	set 6
$m_{T,W}$ upper border [GeV]	set 7
$\not{E}_T$ [GeV]	set 8
m_W [GeV]	set 9
all variable cuts	set 10

Table 6.9.: The combinations of variable- and observable cuts. Set 4 to set 9 are purposed to study the effect of each cut alone, set 10 combines all cuts.

	electron		muon		
Observable	R_{signal} [%]	R_{SC} [%]	R_{signal} [%]	R_{SC} [%]	
m_t [GeV]	41.95	96.30	41.58	97.15	
D_{32} [GeV]	42.08	96.25	41.67	97.11	
R_{32} [-]	42.11	96.26	41.70	97.10	set 10
$m_{\ell b}$ [GeV]	41.87	96.30	41.45	97.12	
R_{diff} [-]	42.11	96.25	41.71	97.10	

Systematics	m_t	D_{32}	R_{32}	R_{diff}	$m_{\ell b}$
electron					
Radiation [GeV]	±4.7*	±2.66	±2.05	±2.68	±1.61
Statistical uncertainty [GeV]	±0.47	±0.35	±0.49	±0.35	±0.54
Total uncertainty [GeV]	±4.72*	±2.69	±2.11	±2.70	±1.70
muon					
Radiation [GeV]	±3.51	±2.28	±1.74	±2.26	±1.11
Statistical uncertainty [GeV]	±0.39	±0.28	±0.38	±0.30	±0.52
Total uncertainty [GeV]	±3.53	±2.29	±1.78	±2.28	±1.22

Table 6.10.: The ratios and uncertainties with set 10 applied. Values labelled with a star are calculated in such a setting without results $\Gamma = 0\,\text{GeV}$.

	electron		muon		
Observable	R_{signal} [%]	R_{SC} [%]	R_{signal} [%]	R_{SC} [%]	
m_t [GeV]	77.27	91.11	75.95	92.17	
D_{32} [GeV]	77.48	91.07	76.14	92.12	
R_{32} [-]	74.75	91.33	73.15	92.36	set 4
$m_{\ell b}$ [GeV]	77.10	91.13	75.73	92.14	
R_{diff} [-]	77.59	91.06	76.17	92.12	

	electron		muon		
Observable	R_{signal} [%]	R_{SC} [%]	R_{signal} [%]	R_{SC} [%]	
m_t [GeV]	82.43	94.00	81.92	95.44	
D_{32} [GeV]	82.42	94.02	81.87	95.50	
R_{32} [-]	80.43	94.07	79.87	95.54	set 5
$m_{\ell b}$ [GeV]	84.63	94.02	84.04	95.45	
R_{diff} [-]	82.59	94.01	82.03	95.48	

	electron		muon		
Observable	R_{signal} [%]	R_{SC} [%]	R_{signal} [%]	R_{SC} [%]	
m_t [GeV]	82.77	89.36	83.68	90.30	
D_{32} [GeV]	82.55	89.48	83.42	90.51	
R_{32} [-]	81.58	89.37	82.45	90.38	set 6
$m_{\ell b}$ [GeV]	86.57	89.16	87.45	90.17	
R_{diff} [-]	82.73	89.46	83.60	90.48	

	electron		muon		
Observable	R_{signal} [%]	R_{SC} [%]	R_{signal} [%]	R_{SC} [%]	
m_t [GeV]	92.22	88.67	92.10	89.83	
D_{32} [GeV]	91.97	88.79	91.82	89.99	
R_{32} [-]	90.91	88.70	90.76	89.89	set 7
$m_{\ell b}$ [GeV]	96.41	88.48	96.21	89.66	
R_{diff} [-]	92.16	88.76	92.01	89.97	

	electron		muon		
Observable	R_{signal} [%]	R_{SC} [%]	R_{signal} [%]	R_{SC} [%]	
m_t [GeV]	89.73	88.66	89.98	89.85	
D_{32} [GeV]	89.51	88.77	89.71	90.01	
R_{32} [-]	88.34	88.68	88.54	89.93	set 8
$m_{\ell b}$ [GeV]	93.71	88.47	93.89	89.70	
R_{diff} [-]	89.69	88.74	89.89	89.99	

	electron		muon		
Observable	R_{signal} [%]	R_{SC} [%]	R_{signal} [%]	R_{SC} [%]	
m_t [GeV]	60.29	91.02	60.01	91.95	
D_{32} [GeV]	59.25	91.28	58.97	92.21	
R_{32} [-]	59.89	91.14	59.61	92.08	set 9
$m_{\ell b}$ [GeV]	61.10	91.04	60.80	91.98	
R_{diff} [-]	59.35	91.25	59.07	92.19	

Table 6.11.: The ratios calculated for the sets 4 to 9.

Systematic	m_t	D_{32}	R_{32}	R_{diff}	$m_{\ell b}$	channel	Set
Radiation [GeV]	±4.50	±3.22	±3.41	±3.26	±1.40		
Statistical uncertainty [GeV]	±0.59	±0.41	±0.57	±0.41	±0.58	electron	
Total uncertainty [GeV]	±4.54	±3.25	±3.46	±3.28	±1.52		4
Radiation [GeV]	±4..37	±2..85	±2.95	±2.86	±1.17		
Statistical uncertainty [GeV]	±0.45	±0.32	±0.46	±0.32	±0.51	muon	
Total uncertainty [GeV]	±4.39	±2.86	±2.99	±2.88	±1.28		
Radiation [GeV]	±4.41	±3.37	±3.55	±3.37	±1.20		
Statistical uncertainty [GeV]	±0.54	±0.40	±0.62	±0.41	±0.59	electron	
Total uncertainty [GeV]	±4.44	±3.39	±3.60	±3.40	±1.34		5
Radiation [GeV]	±4.44	±3.36	±3.40	±3.38	±1.16		
Statistical uncertainty [GeV]	±0.40	±0.34	±0.48	±0.33	±0.46	muon	
Total uncertainty [GeV]	±4.46	±3.37	±3.43	±3.40	±1.25		
Radiation [GeV]	±4.40	±3.32	±3.61	±3.40	±1.09		
Statistical uncertainty [GeV]	±0.59	±0.43	±0.66	±0.44	±0.57	electron	
Total uncertainty [GeV]	±4.44	±3.34	±3.67	±3.43	±1.23		6
Radiation [GeV]	±4.33	±3.21	±3.40	±3..26	±1.30		
Statistical uncertainty [GeV]	±0.44	±0.36	±0.51	±0.36	±0.48	muon	
Total uncertainty [GeV]	±4.35	±3.23	±3.44	±3.28	±1.38		
Radiation [GeV]	±4.42	±3.16	±3.33	±3.19	±1.43		
Statistical uncertainty [GeV]	±0.54	±0.44	±0.65	±0.41	±0.59	electron	
Total uncertainty [GeV]	±4.46	±3.19	±3.39	±3.22	±1.54		7
Radiation [GeV]	±4.42	±3.17	±3.33	±3.22	±1.38		
Statistical uncertainty [GeV]	±0.42	±0.34	±0.48	±0.35	±0.52	muon	
Total uncertainty [GeV]	±4.44	±3.19	±3.37	±3.24	±1.48		
Radiation [GeV]	±4.47	±3.19	±3.31	±3.22	±1.33		
Statistical uncertainty [GeV]	±0.57	±0.44	±0.62	±0.43	±0.62	electron	
Total uncertainty [GeV]	±4.51	±3.22	±3.37	±3.25	±1.47		8
Radiation [GeV]	±4.39	±3.23	±3.43	±3.28	±1.45		
Statistical uncertainty [GeV]	±0.41	±0.36	±0.50	±0.36	±0.49	muon	
Total uncertainty [GeV]	±4.41	±3.25	±3.46	±3.30	±1.53		
Radiation [GeV]	±4.02	±2.66	±2.27	±2.67	±1.65		
Statistical uncertainty [GeV]	±0.48	±0.36	±0.52	±0.37	±0.56	electron	
Total uncertainty [GeV]	±4.05	±2.68	±2.33	±2.69	±1.74		9
Radiation [GeV]	±3.48	±2.49	±2.34	±2.48	±1.20		
Statistical uncertainty [GeV]	±0.33	±0.28	±0.39	±0.27	±0.48	muon	
Total uncertainty [GeV]	±3.49	±2.51	±2.37	±2.49	±1.29		

Table 6.12.: The uncertainties of the sets 4 to 9.

6.6. Optimising Cuts

This chapter will explain how the most effective cuts were optimised. The LL is a measure of the quality of the event reconstruction with KLFitter and has caused improvements of the radiation uncertainty, therefore it is chosen as the variable cut that is to be optimised. The observable that showed the biggest improvements so far is R_{32}. D_{32} showed promising results in other studies, as well. Therefore those two observables will be chosen for the optimisation. Although $m_{\ell b}$ showed promising results, too, it is not considered for a scan because the uncertainty is already low. The optimisation will be conducted via scans of the ranges of the observables and the LL. The first optimisation concerns the logarithmic likelihood, which is conducted for every observable.

6.6.1. Likelihood Scan

The distribution of the logarithmic likelihood for the default cuts including signal and background events are shown in Fig. 6.4.

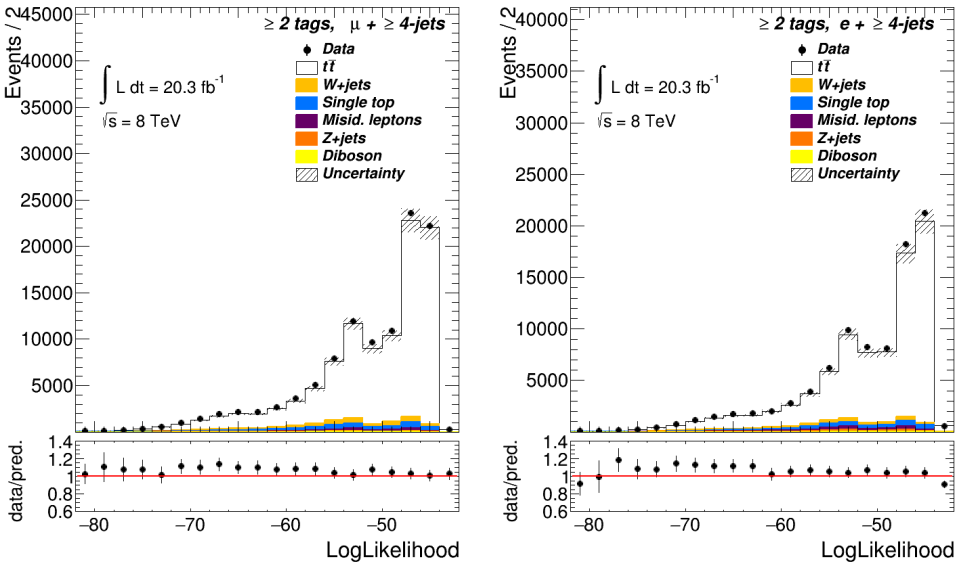

(a) (b)

Figure 6.4.: The default distribution of the LL including signal and background events.

The scan consists of cuts that constrain the LL to domains with lower boundaries of -60 to -50 in steps of two. Lower boundaries than those are not tested because the number of events with $LL < -60$ do not decrease much. To keep a minimum of events, no cuts stricter than $LL > -50$ are tested. Again all of the cuts are applied together

with the observable cuts of set 2. The ratios for all cuts are listed in Tab. 6.13 and the uncertainties in Tab. 6.14.

The ratios R_{SC} improve with every cut stricter than the one before, with only one exception. R_{SC} is slightly better with $LL > -58$ than $LL > -56$ for $m_{\ell b}$ in the muon channel.

Because of instabilities of the fit code many results for D_{32} with $LL > -52$ were set to 0. The listed value corresponds to such a setting without 0 GeV results. Values calculated this way serve only as estimators for the order of magnitude of the uncertainty and are labelled with a star. The best results with respect to the radiation uncertainty and the total uncertainty are achieved with $LL > -50$ for D_{32} and R_{32} in both channels, $LL > -52$ for $m_{\ell b}$ in both channels as well, $LL > -58$ and $LL > -54$ for m_t in the electron- and muon channel, respectively, and $LL > -60$ and $LL > -50$ for R_{diff} for the electron- and muon channel, respectively. As before, the observables behave differently when the cuts are applied.

The results of this scan will be used for the final fits in Ch. 6.7.

6.6.2. Scan for R_{32} and D_{32}

The starting point of both scans are newly chosen cuts that only consider bins which include approximately 1000 events or more. The default distribution of D_{32} and R_{32} are shown in Fig. 6.5 for muons and in Fig. A.1 for electrons. This way the following cuts are chosen:

- $40\,\text{GeV} < D_{32} < 140\,\text{GeV}$
- $1.2 < R_{32} < 2.7$

The observables are scanned upwards and downwards by increasing or decreasing, respectively, the interval between the upper and lower border in regular steps. The interval length of R_{32} will be changed by 0.1 each step. Thus, it will range from interval lengths 0.3 to 2.7, with corresponding cuts:

- smallest interval: $1.9 < R_{32} < 2.2$
- widest interval: $1.0 < R_{32} < 3.7$

D_{32} was scanned mainly in steps of 10 GeV from an interval length of 70 GeV to 350 GeV, defined by the cuts

- smallest interval: $50\,\text{GeV} < D_{32} < 120\,\text{GeV}$

	electron		muon		
Observable	R_{signal} [%]	R_{SC} [%]	R_{signal} [%]	R_{SC} [%]	LL
m_t [GeV]	57.22	92.73	56.29	93.50	
D_{32} [GeV]	57.57	92.71	56.33	93.49	
R_{32} [-]	57.57	92.71	56.33	93.49	> -50
$m_{\ell b}$ [GeV]	57.27	92.73	56.03	93.47	
R_{diff} [-]	57.57	92.71	56.33	93.49	

	electron		muon		
Observable	R_{signal} [%]	R_{SC} [%]	R_{signal} [%]	R_{SC} [%]	LL
m_t [GeV]	66.61	92.08	65.05	93.06	
D_{32} [GeV]	66.69	92.05	65.13	93.03	
R_{32} [-]	65.57	92.17	64.22	93.08	> -52
$m_{\ell b}$ [GeV]	66.34	92.07	64.78	93.03	
R_{diff} [-]	66.69	92.05	65.13	93.03	

	electron		muon		
Observable	R_{signal} [%]	R_{SC} [%]	R_{signal} [%]	R_{SC} [%]	LL
m_t [GeV]	77.27	91.11	75.95	92.17	
D_{32} [GeV]	77.48	91.07	76.14	92.12	
R_{32} [-]	74.75	91.33	73.15	92.36	> -54
$m_{\ell b}$ [GeV]	77.10	91.13	75.73	92.14	
R_{diff} [-]	77.59	91.06	76.17	92.12	

	electron		muon		
Observable	R_{signal} [%]	R_{SC} [%]	R_{signal} [%]	R_{SC} [%]	LL
m_t [GeV]	83.35	90.30	82.58	91.43	
D_{32} [GeV]	83.18	90.28	82.52	91.43	
R_{32} [-]	80.37	90.53	79.66	91.65	> -56
$m_{\ell b}$ [GeV]	83.27	90.34	82.46	91.41	
R_{diff} [-]	83.32	90.26	82.64	91.41	

	electron		muon		
Observable	R_{signal} [%]	R_{SC} [%]	R_{signal} [%]	R_{SC} [%]	LL
m_t [GeV]	86.67	89.75	86.20	90.91	
D_{32} [GeV]	85.78	89.87	85.40	91.02	
R_{32} [-]	83.24	90.04	82.82	91.18	> -58
$m_{\ell b}$ [GeV]	86.81	89.84	86.27	91.94	
R_{diff} [-]	85.94	89.84	85.55	91.01	

	electron		muon		
Observable	R_{signal} [%]	R_{SC} [%]	R_{signal} [%]	R_{SC} [%]	LL
m_t [GeV]	88.61	89.48	88.28	90.62	
D_{32} [GeV]	87.55	89.62	87.22	90.79	
R_{32} [-]	85.08	89.77	84.76	90.90	> -60
$m_{\ell b}$ [GeV]	89.34	89.57	88.88	90.65	
R_{diff} [-]	87.72	89.60	87.39	90.77	

Table 6.13.: The ratios for all sets of cuts in the LL scan.

Systematic	m_t	D_{32}	R_{32}	R_{diff}	$m_{\ell b}$	channel	LL cut
Radiation [GeV]	±7.77	±3.15	±3.00	±3.14	±1.51	electron	> -50
Statistical uncertainty [GeV]	±0.62	±0.42	±0.63	±0.41	±0.63		
Total uncertainty [GeV]	±7.80	±3.18	±3.07	±3.16	±1.63		
Radiation [GeV]	±4.45	±2.78	±2.83	±2.81	±0.83	muon	
Statistical uncertainty [GeV]	±0.50	±0.34	±0.53	±0.35	±0.53		
Total uncertainty [GeV]	±4.48	±2.80	±2.88	±2.83	±0.98		
Radiation [GeV]	±7.17	±2.9*	±3.16	±2.70	±1.50	electron	> -52
Statistical uncertainty [GeV]	±0.62	±0.33	±0.62	±0.43	±0.68		
Total uncertainty [GeV]	±7.20	±2.92*	±3.22	±2.73	±1.64		
Radiation [GeV]	±4.39	±3.3*	±2.94	±2.02	±1.05	muon	
Statistical uncertainty [GeV]	±0.50	±0.41	±0.53	±0.33	±0.54		
Total uncertainty [GeV]	±4.42	±3.33*	±2.99	±2.05	±1.18		
Radiation [GeV]	±4.50	±3.22	±3.41	±3.26	±1.40	electron	> -54
Statistical uncertainty [GeV]	±0.59	±0.41	±0.57	±0.41	±0.58		
Total uncertainty [GeV]	±4.54	±3.25	±3.46	±3.28	±1.52		
Radiation [GeV]	±4.37	±2.85	±2.95	±2.86	±1.17	muon	
Statistical uncertainty [GeV]	±0.45	±0.32	±0.46	±0.32	±0.51		
Total uncertainty [GeV]	±4.39	±2.86	±2.99	±2.88	±1.28		
Radiation [GeV]	±4.57	±3.20	±3.58	±3.21	±1.42	electron	> -56
Statistical uncertainty [GeV]	±0.57	±0.42	±0.59	±0.42	±0.61		
Total uncertainty [GeV]	±4.61	±3.22	±3.63	±3.24	±1.54		
Radiation [GeV]	±4.47	±2.99	±3.34	±2.99	±1.26	muon	
Statistical uncertainty [GeV]	±0.45	±0.33	±0.46	±0.33	±0.49		
Total uncertainty [GeV]	±4.49	±3.01	±3.37	±3.01	±1.35		
Radiation [GeV]	±4.35	±3.18	±3.60	±3.21	±1.30	electron	> -58
Statistical uncertainty [GeV]	±0.56	±0.42	±0.61	±0.44	±0.62		
Total uncertainty [GeV]	±4.39	±3.20	±3.66	±3.24	±1.44		
Radiation [GeV]	±4.42	±3.08	±3.27	±3.08	±1.32	muon	
Statistical uncertainty [GeV]	±0.43	±0.34	±0.47	±0.33	±0.50		
Total uncertainty [GeV]	±4.44	±3.10	±3.30	±3.10	±1.41		
Radiation [GeV]	±4.42	±3.18	±3.52	±3.21	±1.25	electron	> -60
Statistical uncertainty [GeV]	±0.58	±0.45	±0.61	±0.44	±0.60		
Total uncertainty [GeV]	±4.45	±3.21	±3.57	±3.24	±1.39		
Radiation [GeV]	±4.50	±3.09	±3.20	±3.09	±1.45	muon	
Statistical uncertainty [GeV]	±0.42	±0.34	±0.48	±0.34	±0.49		
Total uncertainty [GeV]	±4.52	±3.10	±3.23	±3.11	±1.53		

Table 6.14.: The uncertainties of all sets included in the LL scan.

- widest interval: $0\,\text{GeV} < D_{32} < 350\,\text{GeV}$

The latter cut is the default cut on D_{32}, too. The steps of 10 GeV are continued to the cut $0\,\text{GeV} < D_{32} < 220\,\text{GeV}$. Due to a clear tendency of the uncertainty of the fit result to decrease with an increasing interval length, the step size was increased to 20 GeV. Between the two widest cuts is a gap in length of 30 GeV.

While scanning downwards for R_{32}, the uncertainty kept decreasing, thus the scan was continued to the narrowest interval mentioned above. However the fit became more unstable, for a decreasing amount of statistics. To a certain degree, this problem can be solved through rebinning the histograms as before. Thus, the best cut is chosen, considering not only the uncertainty, but also the stability of the fit. The resulting total uncertainties for both channels are plotted as a function of the interval length in Fig. 6.6.

The reason why the uncertainty for R_{32} gets smaller for narrower cuts is given by the behaviour of the radiation samples in the tail of the distribution. Choosing a narrow interval cuts off fluctuations of the ratio of the nominal sample and the radiation samples. For D_{32} those fluctuations are slower and can partially compensate the deviations of the radiation samples in the peak of the distribution, which is the reason for their different behaviour shown in Fig. 6.6. The fluctuations in the behaviour of the graph are caused by the discontinuous distribution, the finite binning, respectively, of the observables.

The results of the observable scan for D_{32} and R_{32} are therefore

- $0\,\text{GeV} < D_{32} < 350\,\text{GeV}$
- $1.4 < R_{32} < 2.5$

For narrower cuts on R_{32}, the fit might get unstable, especially if further cuts are applied, that would reduce the number of events even more. Detailed information about the cuts are listed in Tab. 6.15.

	electron		muon	
	D_{32}	R_{32}	D_{32}	R_{32}
Radiation [GeV]	±2.63	±3.57	±2.46	±3.37
Statistical uncertainty [GeV]	±0.42	±0.75	±0.35	±0.60
Total uncertainty [GeV]	±2.66	±3.64	±2.49	±3.43
R_{signal} [%]	100	76.50	100	76.46
R_{SC} [%]	87.75	89.89	89.03	90.94

Table 6.15.: The uncertainties of the best cuts of the observable scans and their ratios.

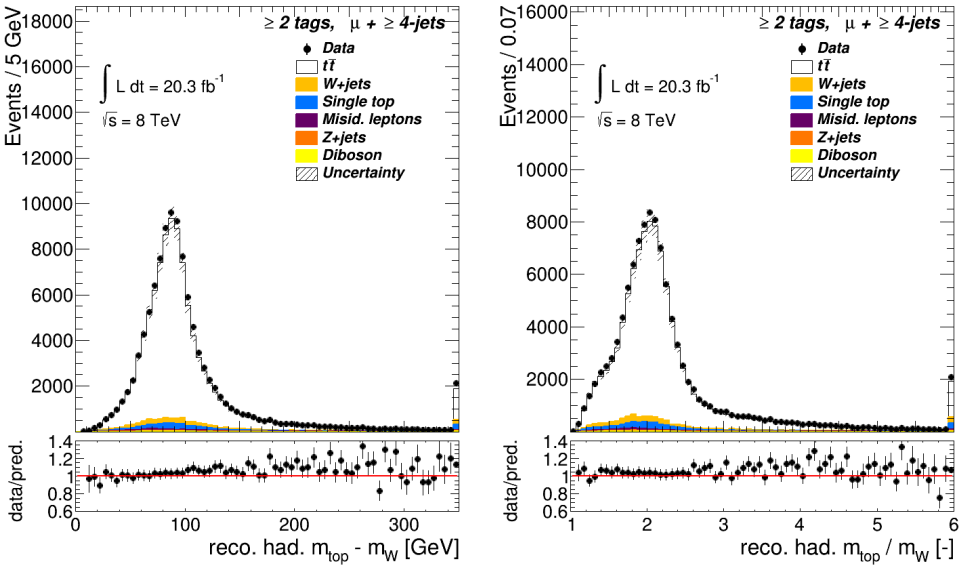

Figure 6.5.: The default distributions of D_{32} and R_{32} in the muon channel.

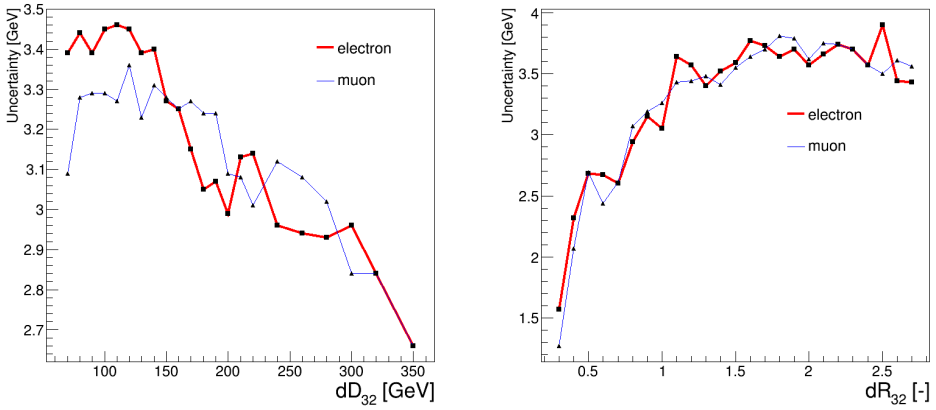

Figure 6.6.: The uncertainties of the fit result as a function of the interval length of the corresponding cuts. They are plotted for the electron- and muon channel.

	electron		muon	
Observable	R_{32}	D_{32}	R_{32}	D_{32}
Radiation [GeV]	±1.88	±2.78	±1.86	±2.33
Statistical uncertainty [GeV]	±0.62	±0.42	±0.60	±0.36
Total uncertainty [GeV]	±1.98	±2.81	±1.96	±2.36
R_{signal} [%]	36.52	37.74	36.26	37.37
R_{SC} [%]	96.86	96.70	97.50	97.50

Table 6.16.: Uncertainties and ratios of the optimised observable cuts combined with the optimised LL cut and the cuts on the other variables.

At last, D_{32} and R_{32} are fitted with the LL cut found in Ch. 6.6.1 and the other variable cuts introduced in Ch. 6.4. The result of the fit is shown in Tab. 6.16.

Applying the cuts produces the purest sample for both observables so far. The cuts reduced the uncertainties for R_{32} strongly. For D_{32} the radiation uncertainty has increased for the electron channel in comparison with set 1, set 10 and the fit with only the observable cut applied as well. In the muon channel the uncertainty is lower than the uncertainty from set 1, but still larger than the uncertainty from set 10. Therefore, both observables show different behaviour once again, if the observable cuts are applied together with the variable cuts. The dependence of the result on the individual settings of each observable makes it hard to find a good set of cuts.

All cuts found by scanning and the remaining variable cuts are applied to a simultaneous fit in the next chapter.

6.7. Simultaneous Fits

The fit code that was used up to now, can be expanded to fit both channels and each in the 1 exclusive and 2 inclusive b-tag bin at the same time. Because of time constraints further studies with this code are not part of this thesis, it will be introduced as an outlook for the following steps of the analysis. The fit was performed using the optimised cuts on D_{32} and R_{32}. The templates of the fit are shown in Fig. 6.7. The constraints on the variables cut off the tails of the D_{32} distribution.

The result of the fit is listed in Tab. 6.17. The results for both observables surpass every result so far. Therefore, the simultaneous fit is a possibility to reduce the uncertainties even further.

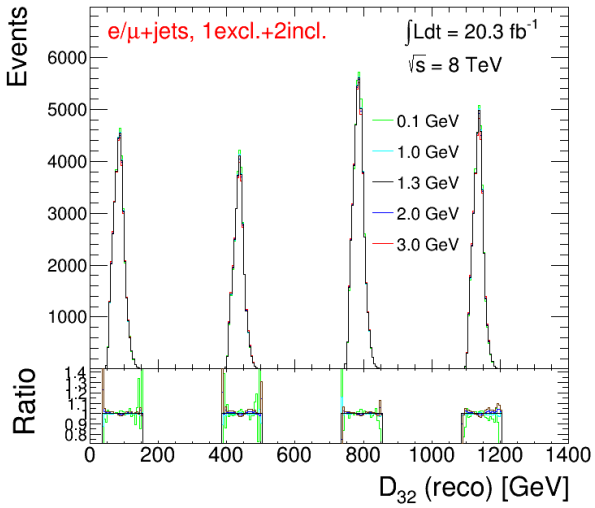

(a)

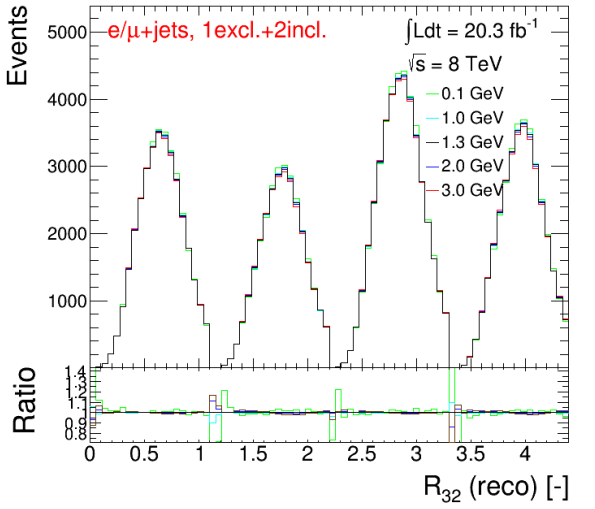

(b)

Figure 6.7.: Selected templates of the simultaneous fit for (a) D_{32} and (b) R_{32}.

Observable	R_{32}	D_{32}
Radiation [GeV]	± 1.36	± 1.97
Statistical uncertainty [GeV]	± 0.36	± 0.22
Total uncertainty [GeV]	± 1.40	± 1.98

Table 6.17.: Uncertainties from the simultaneous fit of both channels and b-tag bins.

7. Conclusion

In this bachelor thesis, several possibilities to reduce the uncertainty on the amount of initial and final state radiation, which is the largest systematic uncertainty in a direct measurement of the top quark decay width, were studied. In this sense it was a feasibility study.

At the beginning, the 1D fit code used in the analysis had to be validated. This was accomplished by the use of calibration curves, comparing the output width of the fit and the width that was used to create the pseudo-data, and pull distributions. Both showed slight deviations from the expectation, which could be explained with the restriction of the fitted width to be non-negative. Therefore, the fit code was proven to be stable.

The first attempt to reduce the radiation uncertainty was to define boundaries for the observables. The boundaries were chosen on the basis of deviations between the nominal sample and the radiation-up and radiation-down sample. They could not reduce the uncertainty, though, but improve the purity of the sample.

In consequence, variable cuts were chosen following the same scheme as for the observable cuts. They were applied together with the observable cuts to exploit the increased purity of the sample. Cutting on the reconstructed W mass, the transverse mass of the W boson, the transverse momentum of the jets, the missing transverse energy and the logarithmic likelihood together with the observable cuts produced the best results so far.

Realising the good effect of the likelihood cut, while the likelihood is also a measure of the quality of the reconstruction of an event, a scan was performed to find the optimal cut for each observable. Further scans were performed for R_{32} which showed the largest improvement of all observables and D_{32} which shows promising results in other studies. Each observable scan contains over 20 different cuts.

In the end, the optimised cuts were applied together with the other variable cuts that showed an improvement of the uncertainty. With those cuts was on one hand the standard fit performed on the other hand a simultaneous fit, recently developed. While the uncertainty for R_{32} could be reduced using the standard fit with the optimised cuts, the uncertainty for D_{32} increased. This shows their different behaviour, caused by differences in the ratio of the nominal sample and the radiation samples for each observable. However,

the simultaneous fit was able to reduce the radiation uncertainty for both observables, which are the best results so far.

Therefore, it was shown that cuts on observables and kinematic variables can reduce the radiation uncertainty. The simultaneous fit was only performed for one set of cuts and showed very good and promising results. It might be able to reduce the uncertainty even further, it is therefore worth studying it in depth. Due to time constraints this could not be part of this thesis.

In the end, it can be concluded that the goal of this thesis was achieved. I was able to show that cuts on observables and variables can help to decrease the radiation uncertainty, although the result depends on the observable very much. The results can be already used in the the top quark decay width analysis and are therefore part of a very demanding analysis.

A. Additional Plots

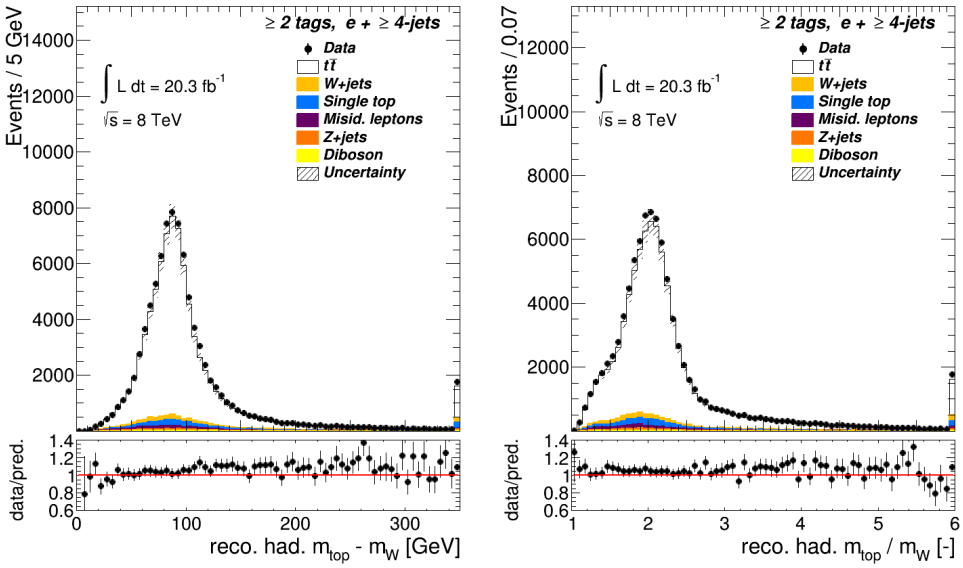

Figure A.1.: The default distributions of D_{32} and R_{32} in the electron channel.

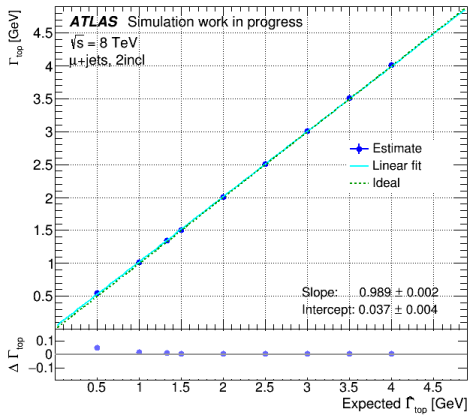

(a)

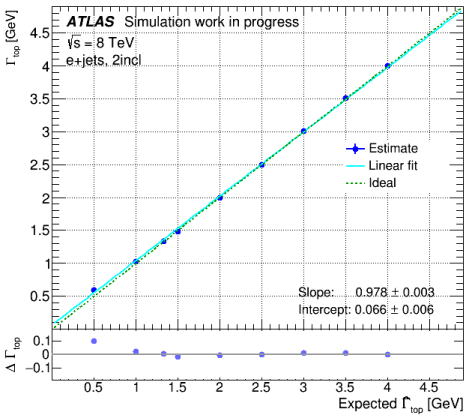

(b)

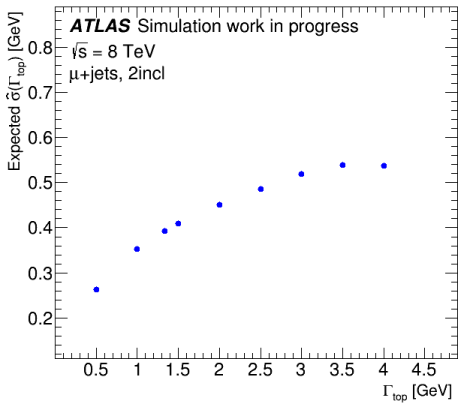

(c)

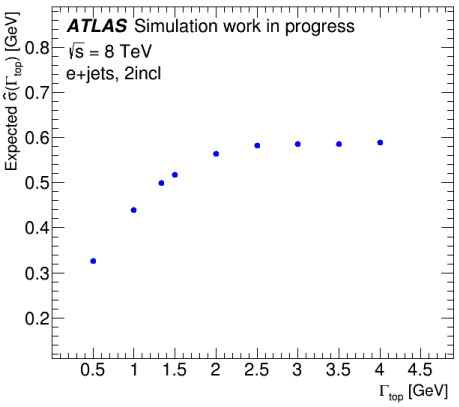

(d)

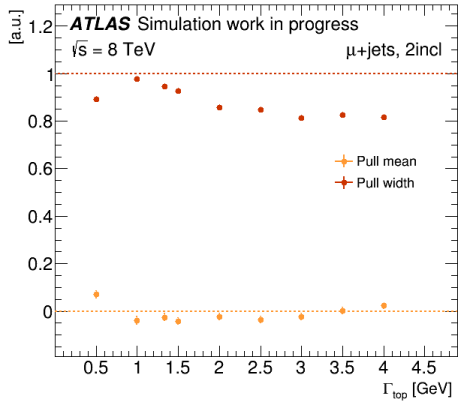

(e)

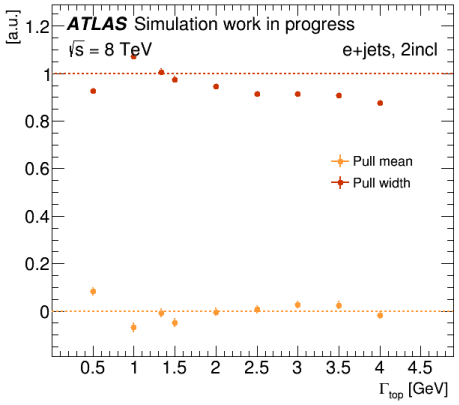

(f)

Figure A.2.: The calibration-, sigma- and pull curves for m_t in the muon channel ((a), (c), (e) respectively) and the electron channel ((b), (d), (f) respectively).

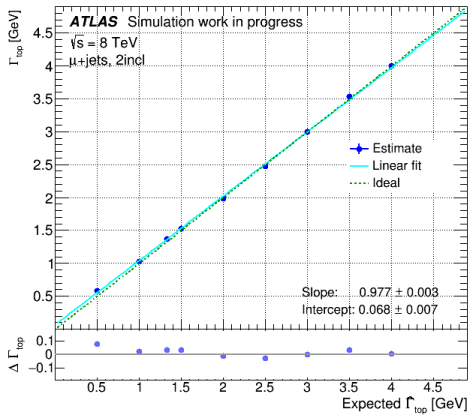

(a)

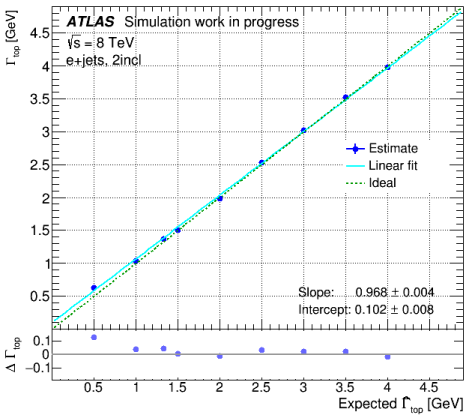

(b)

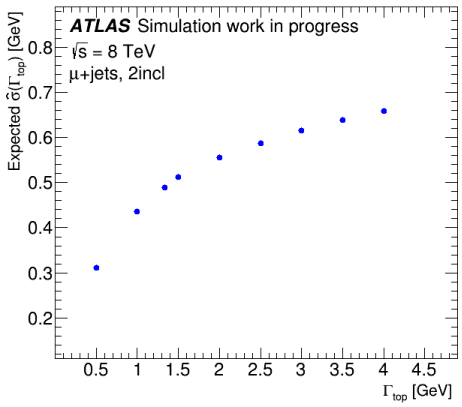

(c)

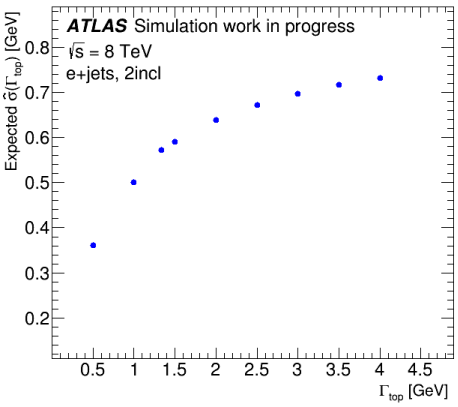

(d)

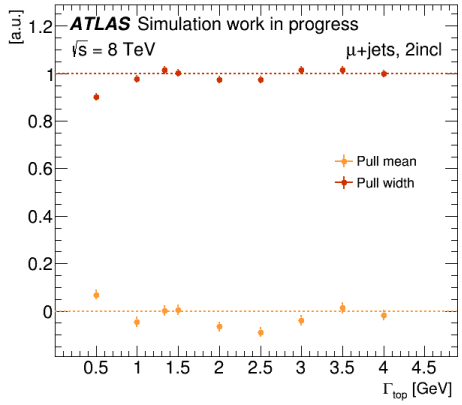

(e)

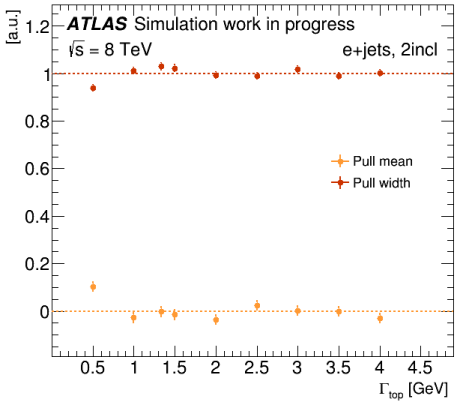

(f)

Figure A.3.: The calibration-, sigma- and pull curves for R_{32} in the muon channel ((a), (c), (e) respectively) and the electron channel ((b), (d), (f) respectively).

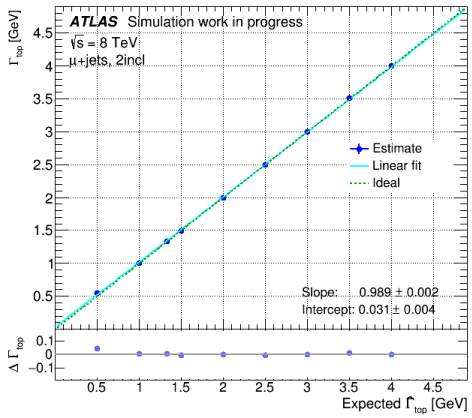

(a)

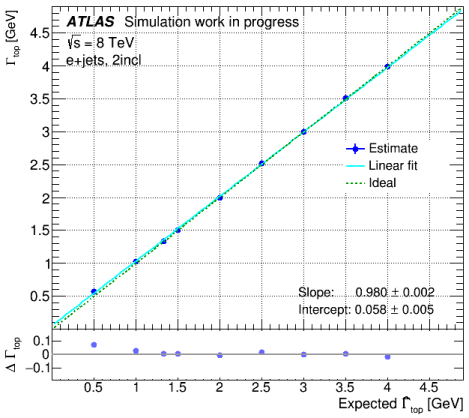

(b)

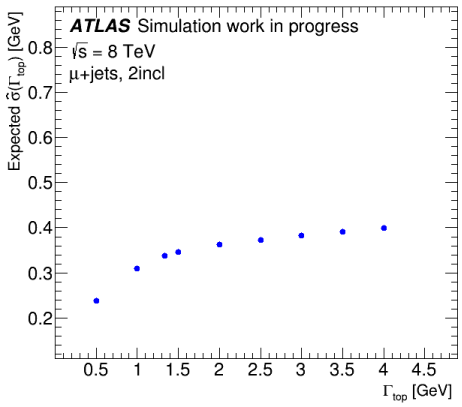

(c)

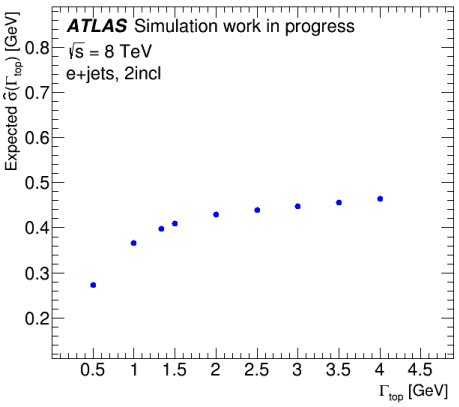

(d)

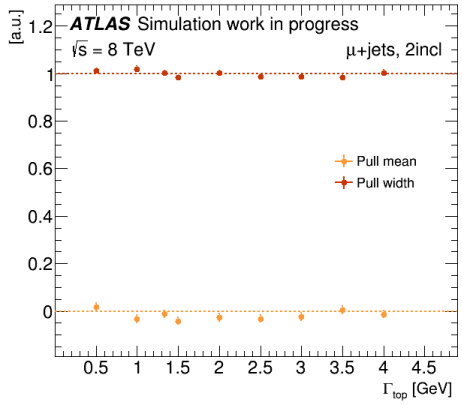

(e)

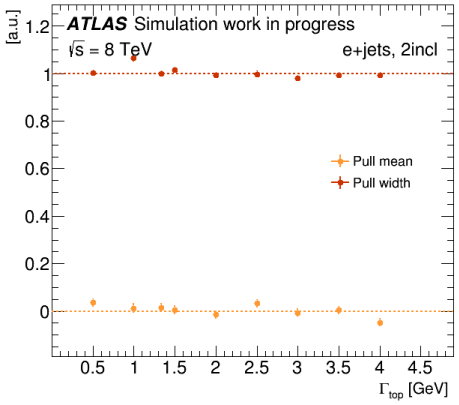

(f)

Figure A.4.: The calibration-, sigma- and pull curves for R_{diff} in the muon channel ((a), (c), (e) respectively) and the electron channel ((b), (d), (f) respectively).

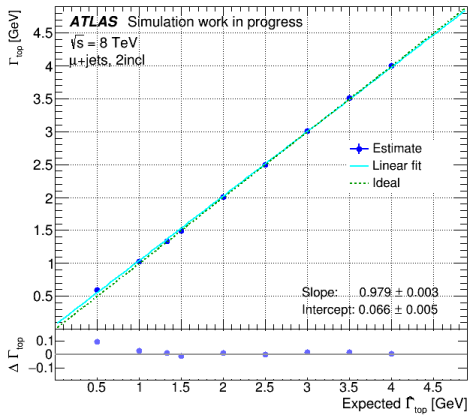

(a)

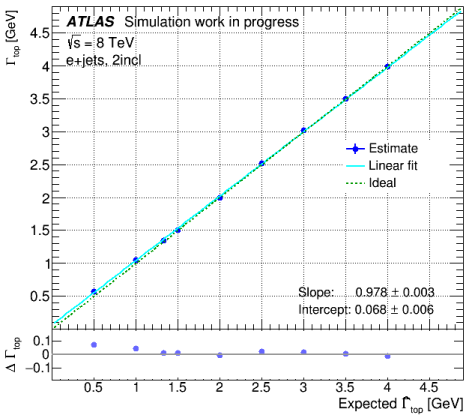

(b)

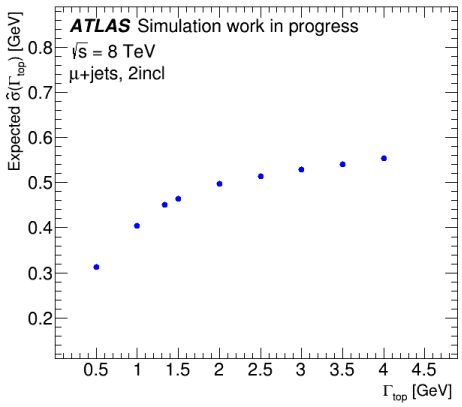

(c)

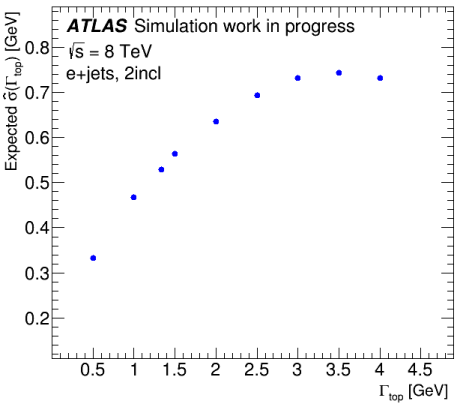

(d)

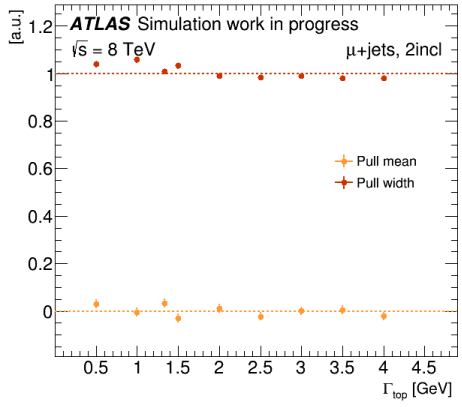

(e)

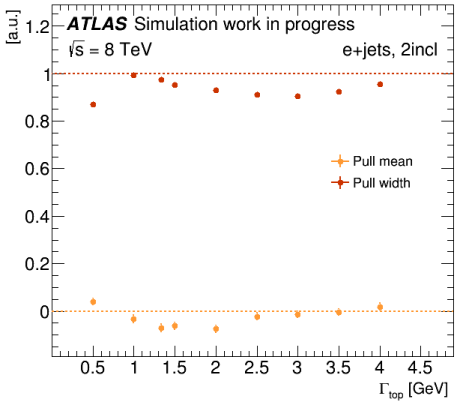

(f)

Figure A.5.: The calibration-, sigma- and pull curves for $m_{\ell b}$ in the muon channel ((a), (c), (e) respectively) and the electron channel ((b), (d), (f) respectively).

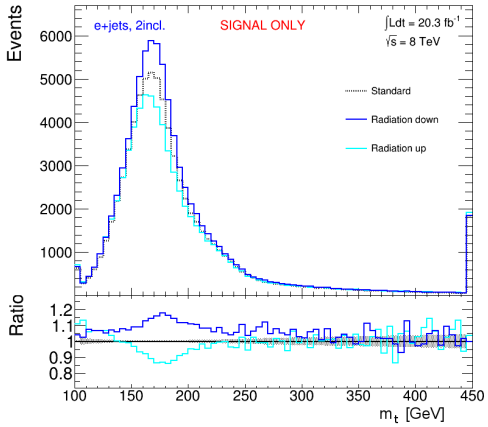

(a)

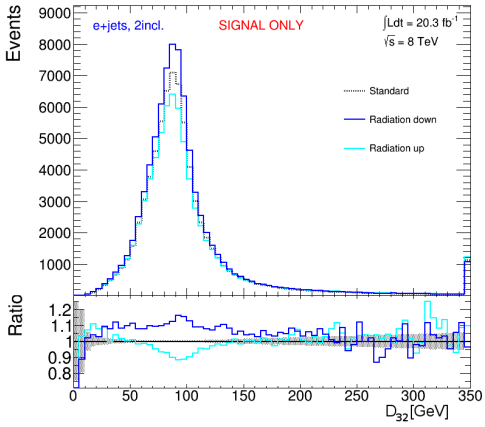

(b)

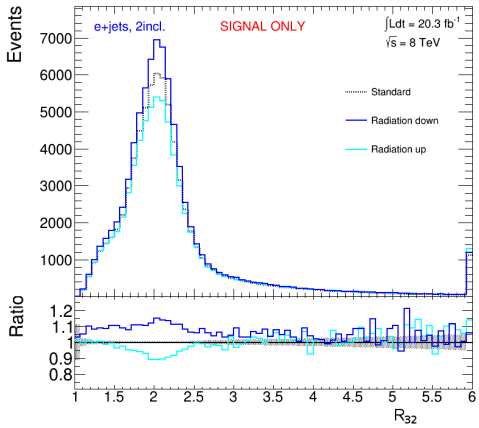

(c)

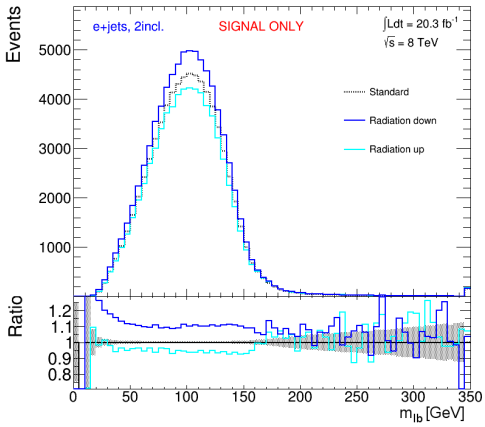

(d)

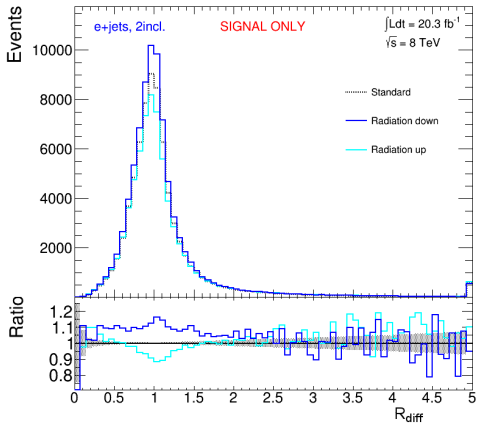

(e)

Figure A.6.: Comparison of the radiation nominal sample with samples assuming higher or lower radiation, for (a) m_t, (b) D_{32}, (c) R_{32}, (d) $m_{\ell b}$ and (e) R_{diff}. All plots contain only the electron channel.

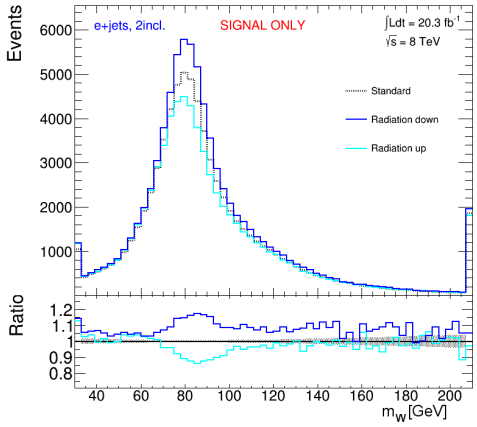

(a)

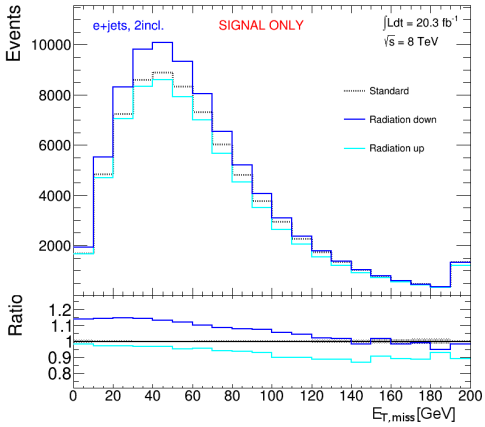

(b)

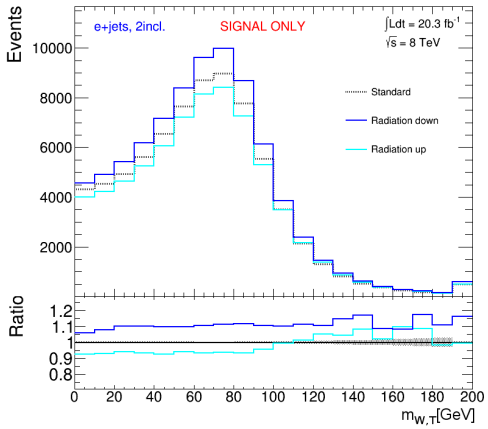

(c)

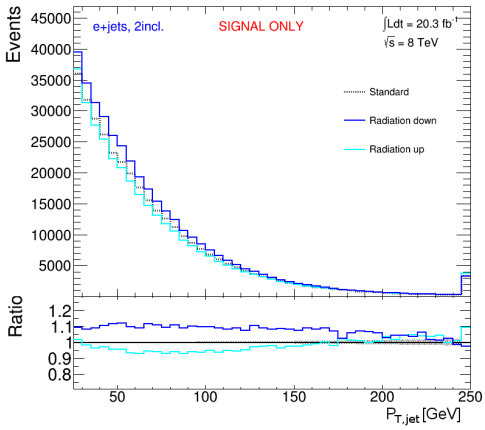

(d)

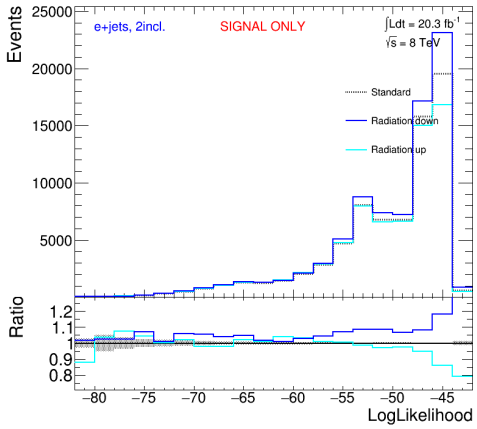

(e)

Figure A.7.: Comparison of the radiation standard sample with sample assuming higher or lower radiation, for (a) m_W, (b) $\not{E}_T$, (c) $m_{T,W}$, (d) $p_{T,\text{jet}}$ and (e) LL. All plots contain only the electron channel.

Bibliography

[1] The CDF Collaboration, *Direct Measurement of the Total Decay Width of the Top Quark*, Phys. Rev. Lett. **111(20)**, 202001 (2013)

[2] S. Weinberg, *A Model of Leptons*, Phys. Rev. Lett. **19**, 1264 (1967)

[3] M. Kobayashi, T. Maskawa, *CP Violation in the Renormalizable Theory of Weak Interaction*, Prog. Theor. Phys. **49**, 652 (1973)

[4] P. W. Higgs, *Broken symmetries, massless particles and gauge fields*, Phys. Lett. **12**, 132 (1964)

[5] The CDF Collaboration, *Observation of top quark production in $\bar{p}p$ collisions*, Phys. Rev. Lett. **74**, 2626 (1995)

[6] The DØ Collaboration, *Observation of the top quark*, Phys. Rev. Lett. **74**, 2632 (1995)

[7] Tevatron Electroweak Working Group (CDF, D0), *Combination of CDF and D0 results on the mass of the top quark using up to 9.7 fb^{-1} at the Tevatron* (2014), 1407.2682

[8] K. A. Olive, et al. (Particle Data Group), *Review of Particle Physics*, Chin. Phys. **C38**, 090001 (2014)

[9] The CMS Collaboration, *Measurement of the ratio $\mathcal{B}(t \to Wb)/\mathcal{B}(t \to Wq)$ in pp collisions at $\sqrt{s}$ = 8 TeV*, Phys. Lett. **B736**, 33 (2014)

[10] A. D. Martin, et al., *Parton distributions for the LHC*, Eur. Phys. J. **C63**, 189 (2009)

[11] CERN, https://twiki.cern.ch/twiki/bin/view/LHCPhysics/TtbarNNLO, as of 06.07.2016

[12] CERN , http://cds.cern.ch/record/1165534/files/CERN-Brochure-2009-003-Eng.pdf, as of 22.06.2016

[13] The ATLAS Collaboration, *The ATLAS Experiment at the CERN Large Hadron Collider*, JINST **3**, S08003 (2008)

[14] R. Brun, F. Rademakers, *ROOT: An object oriented data analysis framework*, Nucl. Instrum. Meth. **A389**, 81 (1997)

[15] W. Verkerke, D. P. Kirkby, *The RooFit toolkit for data modeling*, eConf **C0303241**, MOLT007 (2003)

[16] The ATLAS Collaboration, *Calibration of the performance of b-tagging for c and light-flavour jets in the 2012 ATLAS data*, ATLAS-CONF-2014-046 (2014)

[17] The ATLAS Collaboration, *Measurement of the top quark-pair production cross section with ATLAS in pp collisions at* $\sqrt{s} = 7$ *TeV*, Eur. Phys. J. **C71**, 1577 (2011)

[18] S. Frixione, P. Nason, C. Oleari, *Matching NLO QCD computations with Parton Shower simulations: the POWHEG method*, JHEP **11**, 070 (2007)

[19] T. Sjostrand, S. Mrenna, P. Z. Skands, *PYTHIA 6.4 Physics and Manual*, JHEP **05**, 026 (2006)

[20] M. L. Mangano, et al., *ALPGEN, a generator for hard multiparton processes in hadronic collisions*, JHEP **07**, 001 (2003)

[21] T. Gleisberg, et al., *Event generation with SHERPA 1.1*, JHEP **02**, 007 (2009)

[22] J. Erdmann, et al., *A likelihood-based reconstruction algorithm for top-quark pairs and the KLFitter framework*, Nucl. Instrum. Meth. **A748**, 18 (2014)

[23] F. James, M. Roos, *Minuit: A System for Function Minimization and Analysis of the Parameter Errors and Correlations*, Comput. Phys. Commun. **10**, 343 (1975)

[24] The ATLAS Collaboration (ATLAS), *Jet energy measurement with the ATLAS detector in proton-proton collisions at* $\sqrt{s} = 7$ *TeV*, Eur. Phys. J. **C73(3)**, 2304 (2013)

[25] The ATLAS Collaboration, *Calibrating the b-Tag Efficiency and Mistag Rate in* $35\,\mathrm{pb}^{-1}$ *of Data with the ATLAS Detector*, ATLAS-CONF-2011-089 (2011)

[26] The ATLAS Collaboration, *Measurement of the W Boson Helicity Fractions in* $t\bar{t}$ *Events at* $\sqrt{s} = 8$ *TeV in the Lepton+Jets Channel with ATLAS*, ATLAS-TOP-2016-02 (2016)

[27] The ATLAS Collaboration, *Muon reconstruction efficiency and momentum resolution of the ATLAS experiment in proton-proton collisions at* $\sqrt{s}$ *= 7 TeV in 2010*, Eur. Phys. J. **C74(9)**, 3034 (2014)

[28] CERN, https://twiki.cern.ch/twiki/bin/viewauth/AtlasProtected/TopMC12DiTopSamples, as of 06.07.2016

Acknowledgements

First of all, I want to thank Philipp Stolte who helped to supervise my work the last months. He invested a lot of effort and time in answering my questions whenever I had some, helping me to find bugs in the code and proof-reading my thesis. His effort cannot be appreciated enough.

Next I would like to thank Prof. Dr. Arnulf Quadt for giving me the chance to write my bachelor thesis in his group and being my supervisor and the first referee of it. Moreover I want to thank Prof. Dr. Ariane Frey for being the second referee.

My sincere thanks go to Dr. Boris Lemmer for helpful suggestions and proof-reading of this thesis.

I also want to thank everyone of the Göttingen Top Group, who gave me constructive suggestions during the weekly status reports.

Last but not least, I want to thank my family and friends for giving me mental support the last months.

Erklärung nach §13(9) der Prüfungsordnung für den Bachelor-Studiengang Physik und den Master-Studiengang Physik an der Universität Göttingen:

Hiermit erkläre ich, dass ich diese Abschlussarbeit selbständig verfasst habe, keine anderen als die angegebenen Quellen und Hilfsmittel benutzt habe und alle Stellen, die wörtlich oder sinngemäß aus veröffentlichten Schriften entnommen wurden, als solche kenntlich gemacht habe.
Darüberhinaus erkläre ich, dass diese Abschlussarbeit nicht, auch nicht auszugsweise, im Rahmen einer nichtbestandenen Prüfung an dieser oder einer anderen Hochschule eingereicht wurde.

Göttingen, den 4. Oktober 2016

(Marcel Niemeyer)